OAK RIDGE NATIONAL LABORATORY LIBRARIES
3 4456 0548419 7

[redacted]

CENTRAL RESEARCH LIBRARY
DOCUMENT COLLECTION

OAK RIDGE NATIONAL LABORATORY
operated by
UNION CARBIDE CORPORATION
for the
U.S. ATOMIC ENERGY COMMISSION

ORNL-TM-1000

FUELS AND MATERIALS DEVELOPMENT PROGRAM QUARTERLY PROGRESS REPORT FOR PERIOD ENDING DECEMBER 31, 1964

DECLASSIFIED
CLASSIFICATION CHANGED TO:
BY AUTHORITY OF: AECM-2104 & 2 BL 8/21/74
BY: BL Rudd

CENTRAL RESEARCH LIBRARY
DOCUMENT COLLECTION
LIBRARY LOAN COPY
DO NOT TRANSFER TO ANOTHER PERSON
If you wish someone else to see this document, send in name with document and the library will arrange a loan.

NOTICE This document contains information of a preliminary nature and was prepared primarily for internal use at the Oak Ridge National Laboratory. It is subject to revision or correction and therefore does not represent a final report.

[redacted]

LEGAL NOTICE

This report was prepared as an account of Government sponsored work. Neither the United States, nor the Commission, nor any person acting on behalf of the Commission:

A. Makes any warranty or representation, expressed or implied, with respect to the accuracy, completeness, or usefulness of the information contained in this report, or that the use of any information, apparatus, method, or process disclosed in this report may not infringe privately owned rights; or

B. Assumes any liabilities with respect to the use of, or for damages resulting from the use of any information, apparatus, method, or process disclosed in this report.

As used in the above, "person acting on behalf of the Commission" includes any employee or contractor of the Commission, or employee of such contractor, to the extent that such employee or contractor of the Commission, or employee of such contractor prepares, disseminates, or provides access to, any information pursuant to his employment or contract with the Commission, or his employment with such contractor.

ORNL-TM-1000

Contract No. W-7405-eng-26

FUELS AND MATERIALS DEVELOPMENT PROGRAM QUARTERLY PROGRESS REPORT FOR PERIOD ENDING DECEMBER 31, 1964

Compiled by

P. Patriarca

FEBRUARY 1965

OAK RIDGE NATIONAL LABORATORY
Oak Ridge, Tennessee
operated by
UNION CARBIDE CORPORATION
for the
U.S. ATOMIC ENERGY COMMISSION

OAK RIDGE NATIONAL LABORATORY LIBRARIES

3 4456 0548419 7

FOREWORD

This is the third quarterly progress report describing work performed at the Oak Ridge National Laboratory for the Fuels and Materials Development Branch, Division of Reactor Development, U. S. Atomic Energy Commission. The specific programs covered are as follows:

Program Title	Person in Charge	Principal Investigator(s)
Fuel Element Development	G. M. Adamson, Jr.	C. F. Leitten, Jr. J. P. Hammond
Mechanical Properties	D. A. Douglas, Jr.	J. R. Weir
Nondestructive Test Development	D. A. Douglas, Jr.	R. W. McClung
Solid Reaction Studies	C. J. McHargue	T. S. Lundy
Zirconium Metallurgy	C. J. McHargue	M. L. Picklesimer

TABLE OF CONTENTS

SUMMARY

1. Fuel Element Development

Thermochemical deposition studies of solid deposits of UO_2 from UF_6 have continued and we have shown it to be possible to consistently obtain such deposits. By varying the oxygen concentrations in the gas mixture, it was possible to obtain variations in the oxide stoichiometry from 2.001 to 2.166.

The conditions required to produce large homogeneous tungsten-rhenium deposits have not yet been determined. With rhenium being easier to reduce than tungsten, its concentration is proportionately higher near the inlet. The addition of argon to the reacting gases improved the homogeneity but lowered the reduction efficiency. Deposition temperatures below 500°C also improved the homogeneity, but again, at the expense of efficiency. Hardness measurements and x-ray diffraction studies of the deposits show that alloying of the tungsten and rhenium occurs at temperatures as low as 500°C. A beta tungsten phase has been identified for the first time in this system.

It has been confirmed that uranium carbides prepared from commercial UO_2 may be sintered at temperatures of 1550°C to high densities and with single-phase structures if uranium silicide is used as a sintering aid. Preliminary results indicate silicon vapor can also act as a sintering aid for uranium carbide.

We have developed a procedure which surmounts the large differences in melting points and provides a method for adding yttrium and rare-earth metals to tungsten. Adding the yttrium as fine powders of yttrium aluminide also results in a much-sought-after fine dispersion of the yttrium.

2. Mechanical Properties

Substructures have been developed in thin-sheet specimens of types 304, 302, and 316 stainless steel by cold working and annealing. In preparation for electron microscope examination, the specimens have been irradiated and some of them have been deformed. Some of the properties observed in these specimens are reported.

The influence of preirradiation heat treatment on the postirradiation elevated-temperature tensile properties of type 304 stainless steel has been investigated. A grain size of ASTM 8 to 10 produced by cold working and annealing at 923°C exhibits at least a factor of 2 better postirradiation ductility than does material annealed at normal heat-treating temperatures. An internally consistent effect of cooling rate was observed for the higher temperature anneals.

The possibility of radiation-induced precipitation producing the low ductility at elevated temperatures in irradiated materials was investigated by irradiating and testing relatively pure copper, nickel, and iron. It is shown that radiation-induced embrittlement occurs in these materials. This is interpreted as evidence that precipitation effects are not necessary in the mechanism for the damage to ductility.

3. Nondestructive Test Development

We are developing new techniques and equipment for the nondestructive evaluation of materials and components. The major emphasis has been on eddy-current, ultrasonic and penetrating-radiation methods.

The mathematical approach using a computer to analyze variations in electromagnetic field parameters has been applied to the problem of a coil encircling a ferromagnetic rod. Continued developments to the phase-sensitive eddy-current instrument include development of a hand-held vibrating probe intended to provide greater sensitivity.

The principal efforts in ultrasonic test development have been on reference standards for tubing inspection. Quantitative procedures are being developed for electric discharge machining of notches in molybdenum alloy tubes, and microscopic and replication techniques are being studied for accurate measurements of the product.

New equipment has been designed and fabricated which will aid the application of gamma ray attenuation techniques to the study of inhomogeneity in fuel rods. We have designed and assembled a photomultiplier calibration system which will enable optimum use of scintillation detectors for specific problems. The system includes a single channel analyzer. Our studies with the x-ray sensitive closed-circuit television

equipment have been directed toward measurement of the detector response to radiation and, by using a specially designed penetrameter, determination of ultimate sensitivity and resolution.

Our work on problem materials has included nickel-, tungsten-, tantalum-, and niobium-base alloys.

4. Solid Reaction Studies

We have measured the volume diffusion coefficients of ^{95}Nb and ^{182}Ta in niobium over the temperature range 878 to 2400°C. High-temperature specimens ($T \geq 1500°C$) were sectioned by conventional lathe and grinding techniques while low-temperature specimens were sectioned by an anodizing and stripping technique previously described. Over a range of more than 10 orders of magnitude in diffusivity, the self-diffusion data is well represented by the equation:

$$D = (1.10 \pm 0.04) \exp\left[-(96{,}100 \pm 1700)/RT\right] \text{ cm}^2/\text{sec} \quad .$$

Upward deviations from this line are explained by short-circuit diffusion in combination with the loss of resolution of the sectioning techniques.

In a limited number of measurements, the diffusivity of ^{182}Ta in niobium was found to be about one-half that of ^{95}Nb in niobium, and the activation energies were about the same. Oxygen contamination within the range 100 to 450 ppm was found to have little or no effect on the self-diffusivity of niobium.

5. Zirconium Metallurgy

An analysis of the problem of controlling texture during mill manufacture of Zircaloy-2 tubing has raised the question as to whether the orientation of the final material is independent of the strain path when a given starting shape and texture is deformed into a given final shape. A limited answer has been obtained in that there is at least one case where the texture can differ by approximately 90° for two particular paths, if a particular starting texture is used and a very specific total shape change undergone. In most cases examined, the texture was

almost independent of the path or the same shape could not be obtained by a second path. The analysis is of particular importance in planning fabrication sequences and reductions for control of texture in Zircaloy-2 tubing.

Assuming that the octahedral shear stress theory of yielding in biaxial stress can be modified to allow a material to have a yield strength in compression twice that in tension, a study has been made of the possible yield stress ellipses for three specific textures in Zircaloy-2 tubing. The results indicate that the texture most common in present day Zircaloy-2 tubing (basal poles concentrated in the tangential direction) is inherently unstable for the condition of bulging in tubing in internal pressure. The texture most resistant to bulging is that having basal poles concentrated in the radial direction. One of the first objectives of the tubing test study will be the experimental determination of the biaxial yield curves.

A new technique (and associated equipment) has been developed for determining the index of refraction (as a function of wavelength) of oxide films formed on zirconium alloy specimens. Stripping of the oxide film is not required, all of the necessary data being determined in reflection at two different angles of incidence of the light beam of the spectrophotometer. Preliminary data have proven the feasibility of the method. Zirconium foil specimens have been anodized at voltages ranging from 50 to 400 v and are currently being irradiated in the ORR. Comparison with an identical unirradiated set will be used to determine the effects of the irradiation on the optical properties of the oxide films in situ.

Six zirconium spheres, 3/8 to 5/8 in. in diameter, have been successfully spark cut from zone-refined, near single-crystal zirconium bar. The spheres will be used to study the optical anisotropy of zirconium and the effects of orientation on oxidation and corrosion.

Several zone refining runs of 10 passes each have been made on short specimens of iodide zirconium to determine the effective distribution coefficients of hafnium and oxygen, the principal contaminants remaining in zone-refined zorconium. Analytical results are not yet complete.

Annealing studies of cold-rolled, zone-refined zirconium are in progress. Evidence has been obtained by metallography for the occurrence of some recrystallization in 24 hr at 150°C and confirmed by x-ray diffraction. A hardness peak was observed in most of the zone-refined materials studied but the reason why is not yet known.

Strip specimens from several parts of a zone-refined bar have been prepared for corrosion testing in 680°F water to examine the effects of impurity and impurity levels on corrosion rates.

1. FUEL ELEMENT DEVELOPMENT

G. M. Adamson, Jr.

The objective of the Fuel Element Development Program remains the development of new or improved fabrication techniques for both complete fuel elements and for fuel or cladding materials. We are studying a variety of materials for both uses, selected to include the more promising ones for use at temperatures over a wide range.

We are presently emphasizing vapor deposition as a fabrication technique. Our ultimate goal is the fabrication of a fuel element by a one-step fuel-conversion process followed by formation of an integral cladding, both using thermochemical deposition methods. To achieve this goal, separate fabrication efforts have been directed toward the preparation of UO_2 as the fuel material and refractory metals such as molybdenum, tungsten alloys, or vanadium alloys as the cladding material.

Improvements in the fabrication of uranium carbide fuels are being sought through the use of sintering aids. These aids must lower the sintering temperature without having deleterious effects on other properties and must be useful with commercially available carbide powders.

A hindrance to the development of highly loaded refractory metal dispersion elements is the poor low-temperature ductility of the potential matrix materials. Scouting tests are being conducted on possible methods for improving these properties.

Deposition of Refractory Uranium Compounds

R. L. Heestand C. F. Leitten, Jr.

We have continued deposition studies to determine the effects of gas composition on the stoichiometry of solid UO_2 deposited from UF_6, oxygen, and hydrogen mixtures. Within the following conditions, it has been shown to be possible to consistently obtain solid deposits of UO_2 similar to that shown in Fig. 1.1: pressure below 3 torr; temperature 1250 to 1300°C; and gas compositions ranging from 9 to 12% O_2, 81 to 86% H_2,

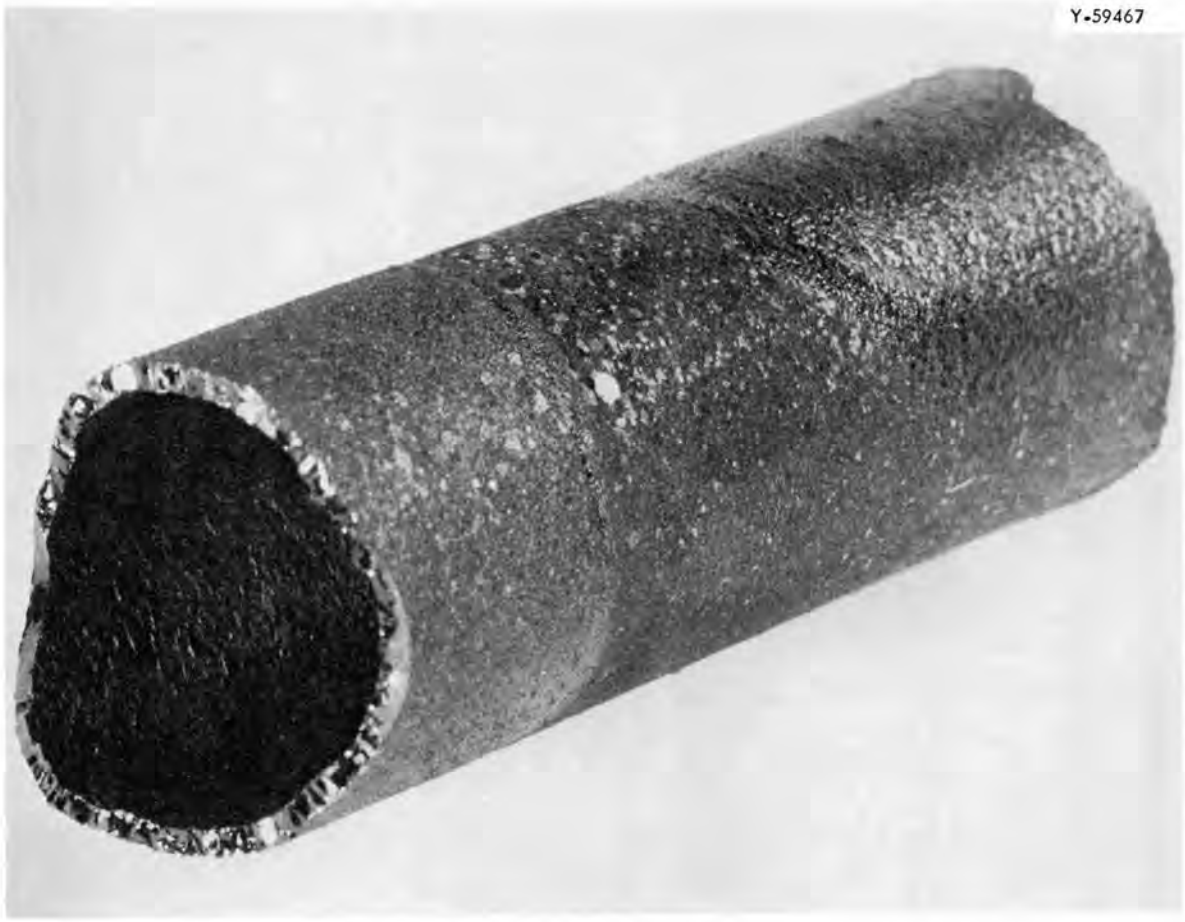

Fig. 1.1. Section of UO_2 Tube, 0.750-in. diam × 0.040-in. Wall, Deposited at 1300°C from UF_6, O_2, and H_2 in 6 hr. 5×.

and 4 to 7% UF_6. With changing concentrations of oxygen, the stoichiometry of the deposit could be varied from 2.001 to 2.166. The resulting changes in structure are shown in Fig. 1.2 as an increasing amount of second phase, probably U_4O_9.

It has been found also that better control of the UF_6 flow rate is necessary if a systematic study of the effects of feed gas composition on the oxygen-to-uranium ratio is to be made. Currently, a heated borosilicate glass flowmeter is in use and small variations in metering temperature give wide variations in the amount of UF_6 transferred. This problem had been circumvented by obtaining the UF_6 cylinder weight loss after each run, thereby providing a value for the average flow rate. The weight balances indicate that for identical flowmeter settings, the amount of UF_6 transferred may vary as much as ±20% in consecutive runs.

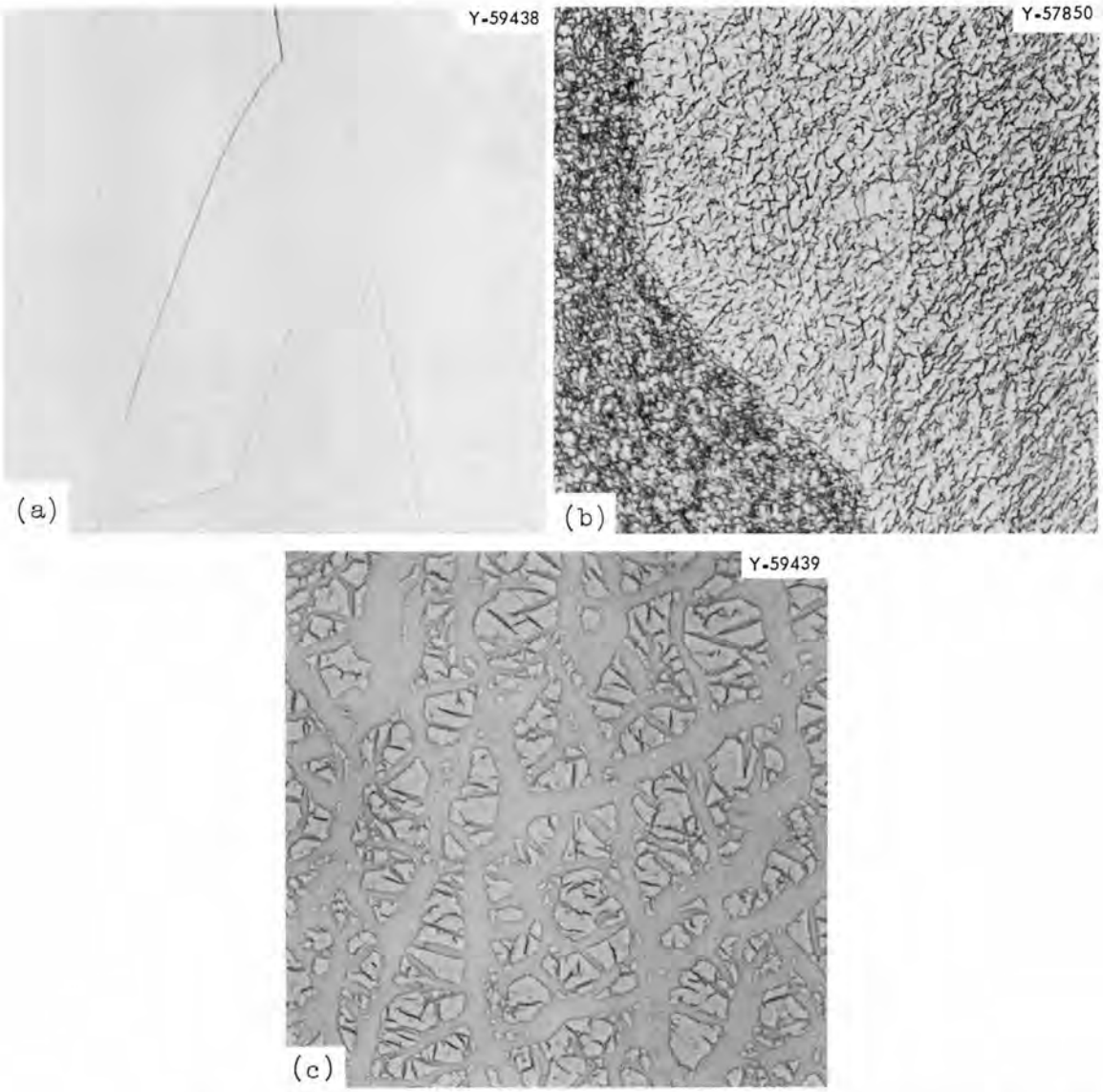

Fig. 1.2. Microstructure of Solid UO_2 Deposits Obtained at 1300°C, 3 Torr for Gas Compositions of: (a) 9% O_2–85% H_2–6% UF_6, oxygen-to-uranium ratio 2.001; (b) 10% steam–86% H_2–4% UF_6, oxygen-to-uranium ratio 2.008; (c) 12% O_2–81% H_2–7% UF_6, oxygen-to-uranium ratio 2.166. Etchant: 70% H_2O, 20% H_2O_2 solution, and 10% concd HNO_3. 250×.

In order to obtain better control of the system variables, mass flowmeters for UF_6 have been ordered and experiments to determine effects of feed gas composition on the oxygen-to-uranium ratio will continue.

Deposition of Tungsten Alloys

J. I. Federer C. F. Leitten, Jr.

Deposition of tungsten-rhenium alloys by hydrogen reduction of tungsten and rhenium hexafluorides and evaluation of the deposits has continued. The objective of this investigation is to determine the conditions which yield homogeneous alloys as tubing and sheet material. Presently, the effects of deposition conditions on homogeneity and uniformity of thickness are being studied in tubular deposits. The alloys are deposited on the inner wall of heated copper tubes using equipment similar to that used for tungsten deposition described elsewhere.[1] Good quality alloy deposits having smooth surface finish have been consistently produced. Problems have been encountered, however, which are unique to the experimental arrangement; that is, a stationary hot zone and the equivalent of a stationary injector at the entrance to the hot zone. The main problem encountered has been nonhomogeneity in the deposits due to the relative ease of reduction of ReF_6 compared to WF_6 as was reported previously.[2] Consequently, the deposits are richer in rhenium near the inlet to the reaction zone than farther downstream. Several composition profiles and corresponding deposition conditions are shown in Fig. 1.3. The recovery values shown were determined by comparing the metal content of both metered fluorides with the weight of deposit obtained in the main deposition furnace. Essentially all fluorides which pass through the main reaction zone are reduced in a scavenger furnace and can be recovered.

---

[1]R. L. Heestand, J. I. Federer, and C. F. Leitten, Jr., Preparation and Evaluation of Vapor-Deposited Tungsten, ORNL-3662 (Aug. 1964).

[2]J. I. Federer and C. F. Leitten, Jr., Fuels and Materials Development Program Quart. Progr. Rept. June 30, 1964, ORNL-TM-920, p. 10.

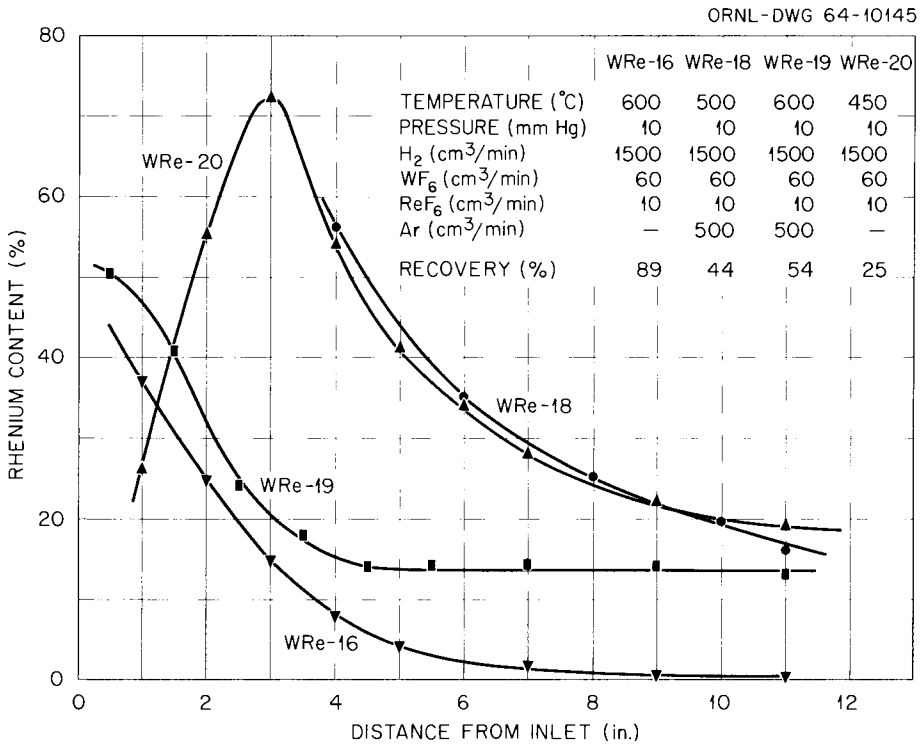

Fig. 1.3. Rhenium Content vs Distance from the Inlet to the Reaction Furnace.

The curve labeled WRe-16 is typical of deposits prepared at temperatures from 500 to 600°C – a high rhenium content near the inlet followed by a rapid decrease in rhenium content with distance from the inlet. The curve labeled WRe-19 represents a deposit prepared at 600°C in which argon was included with the reacting gases. By a mechanism that is not yet completely understood, argon causes the rhenium to be distributed differently throughout the deposit. Comparison with WRe-16 shows that the rhenium content was substantially increased in the "downstream half" of the deposit. In fact, the rhenium content in WRe-19 was essentially constant over the distance 5 to 12 in. from the inlet. The presence of argon, however, did lower the recovery in the main deposition furnace from 89 to 54%. Lowering the deposition temperature to 450°C also caused a significant change in rhenium distribution as shown by the curve labeled WRe-20. The very high rhenium content near the inlet reflects the greater ease of reduction of ReF_6 compared to WF_6 at 450°C. A detailed analysis of the data from several experiments reveals that approximately 80% of the rhenium, but only 55% of the tungsten, was recovered in the main deposition furnace.

Deposition rates for tungsten-rhenium deposits are different from those of unalloyed tungsten as shown in Fig. 1.4. The curve labeled W-600 shows deposition rates as a function of distance from the inlet for unalloyed tungsten deposited at 600°C. In general, the deposition rates for tungsten-rhenium deposits, as typified by curves WRe-16 and -19, are greater near the inlet than for unalloyed tungsten. In addition, comparison of WRe-19 and -16 also shows an apparent suppression of the deposition rates due to the presence of argon.

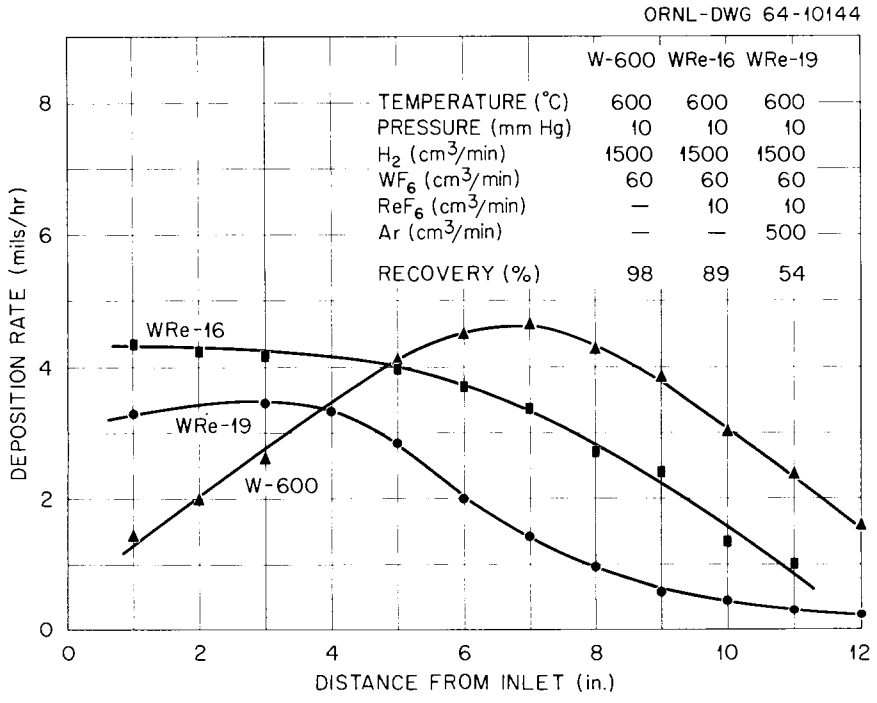

Fig. 1.4. Deposition Rate vs Distance from the Inlet to the Reaction Furnace.

The grain structure of these deposits is generally columnar and appears to be single phase. A W–32% Re alloy is shown in Fig. 1.5. The long columnar grains, having a darker etching constituent at the grain boundaries, are typical of higher rhenium deposits. A W–12% Re alloy is shown in Fig. 1.6. This microstructure, similar to the structure of unalloyed tungsten shown elsewhere,[1] is the usual appearance of deposits containing less than about 25% Re.

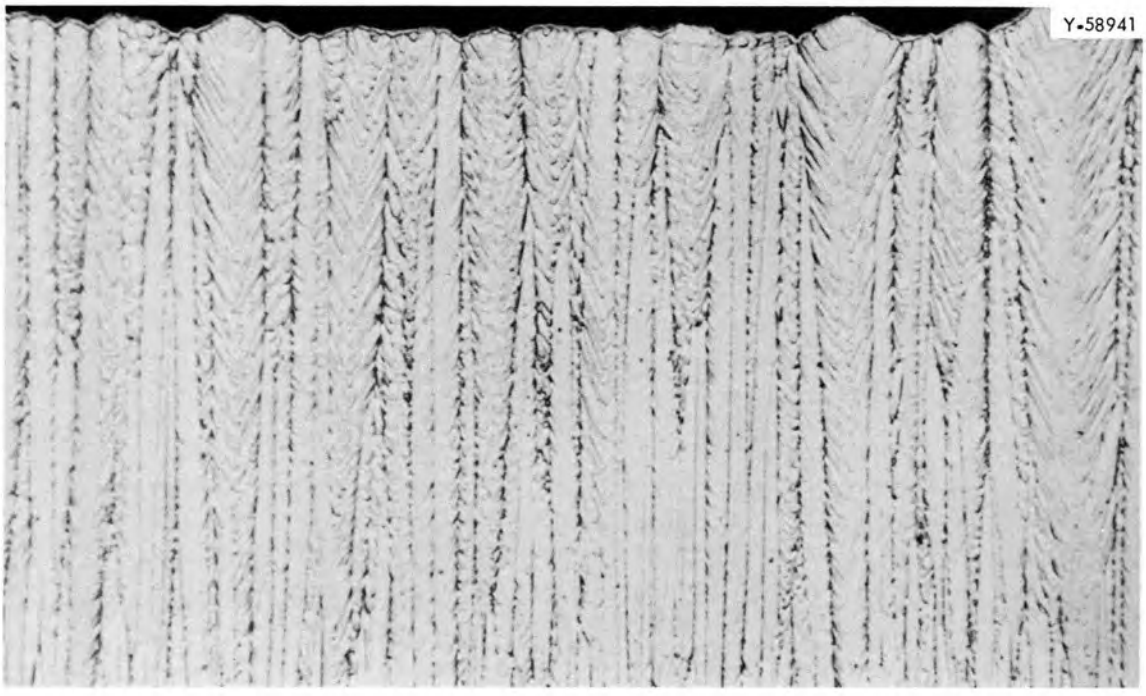

Fig. 1.5. Vapor Deposited W–32% Re Alloy. Etchant: 1 NH_4OH, 1 H_2O_2 (30%), 4 H_2O. 500×.

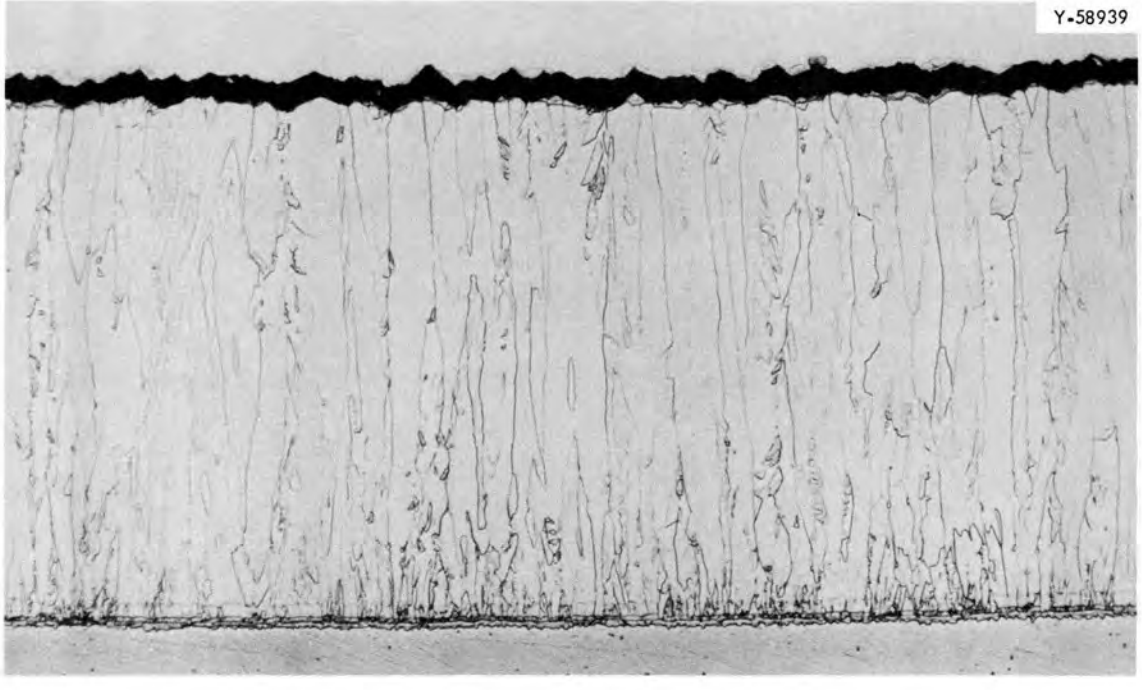

Fig. 1.6. Vapor Deposited W–12% Re Alloy. Etchant: 1 NH_4OH, 1 H_2O_2 (30%), 4 H_2O. 250×.

The interstitial content of two deposits is shown in Table 1.1. In general, the impurity content of these deposits appears to decrease with decreasing rhenium content. Deposits containing greater than 25% Re often degrade during dissolution of the copper deposition tube in nitric acid, reducing the deposit to small pieces having considerable surface discoloration. Thus, the higher oxygen values associated with the higher rhenium content alloys may result from contamination. The data, however, do show the feasibility of producing high-purity tungsten-rhenium deposits by the vapor-deposition process.

Table 1.1. Analysis of Impurities in Tungsten-Rhenium Deposits

Alloy Designation	Temperature (°C)	Distance from Inlet (in.)	Rhenium Content (%)	Impurities,[a] ppm			
				C	H	O	N
WRe-12	500	1	46	120	11	79	9
		3	29	50	8	34	<5
		5	17	<20	2	9	<5
		7	10	<20	2	9	<5
		9	6	<20	2	6	<5
		11	4	<20	2	15	<5
WRe-22	600	1.5	37	<20	3	230	5
		3.5	15	<20	3	30	<5
		5.5	5	20	2	<5	<5
		7.5	2	30	<1	<5	<5
		9.5	1	<20	<1	<5	<5
WRe-23	500	2.5	32	<20	6	34	18
		4.5	19	<20	3	55	6
		6.5	10	<20	1	14	<5
		8.5	5	<20	1	8	<5
		10.5	3	<20	4	41	<5

[a]Limit of detection: 20 ppm.

In addition to chemical analyses and metallographic examination, the deposits are being characterized by x-ray diffraction and hardness measurements. X-ray diffraction patterns were obtained on powder samples of various rhenium contents, and the results are shown in Table 1.2. Two phases were found in as-deposited samples: alpha tungsten (body-centered cubic) which was the principal phase in low rhenium deposits and beta tungsten (cubic) which was favored by high rhenium contents. With decreasing rhenium content, the lattice parameters of the alpha-tungsten phase approach the value for pure tungsten, a_o = 3.1648 A. The beta-tungsten phase is a commonly occurring structure found among intermediate phases involving transition metals. To our knowledge, this is the first

Table 1.2. Results of X-Ray Diffraction Studies on Tungsten-Rhenium Deposits

Powder Sample	Rhenium Content (%)	α-Tungsten		β-Tungsten		Sigma Intensity
		Intensity	a_o(A)	Intensity	a_o(A)	
As-deposited at 600°C	37	NF	NF	S	4.997	NF
	26	W^-	3.144	S	5.010	NF
	15	M	3.152	S	5.018	NF
	4	S^+	3.162	NF	NF	NF
	2	S^+	3.165	NF	NF	NF
	1	S^+	3.165	NF	NF	NF
	<1	S^+	3.165	NF	NF	NF
Annealed at 1500°C for 4 hr	37	M^-	3.146	S	4.996	M^+ {a=9.633 A, c=4.985 A
	26	M	3.146	S	5.011	NF
	15	W^+	3.154	S	5.014	NF
	4	S	3.162	NF	NF	NF
	2	S	3.165	NF	NF	NF
	1	S	3.164	NF	NF	NF
	<1	S	3.165	NF	NF	NF

Legend: S, strong W, weak
M, medium NF, not found

reported occurrence of the phase in the tungsten-rhenium system. The beta-tungsten phase has not been previously reported in phase diagrams, although these diagrams have not been established below a temperature of about 1200°C. Sigma phase, which is reported to occur in alloys containing from 25 to 63% Re, was not found in any of the as-deposited alloys included in this x-ray study. Following a vacuum anneal at 1500°C, the sigma phase was identified in the deposit containing 37% Re. Otherwise, the heat treatment resulted only in small changes of lattice parameters of the deposits. No evidence of elemental rhenium was found in as-deposited or heat-treated samples. Annealing studies are continuing to determine the stability of the microconstituents.

Hardness values of two deposits are shown in Table 1.3. The sharp drop in hardness with decreasing rhenium content coupled with the generally high purity of these deposits supports the x-ray evidence of solid solution or compound formation at the deposition temperatures of 500 and 600°C.

Table 1.3. Hardness of Tungsten-Rhenium Deposits

Alloy Designation	Rhenium Content (%)	Hardness (DPH)
WRe-12	45	1775
	38	1960
	22	1730
	8	570
	5	350
	4	325
WRe-16	37	1680
	26	2000
	8	425
	2	350
	1	380
Unalloyed tungsten	0	450

Thermochemical Deposition of Fine-Grained Tungsten

J. I. Federer C. F. Leitten, Jr.

The purpose of preparing vapor-deposited tungsten containing small additions of other elements is to obtain a finer grain deposit than the columnar structure usually observed. Improvements in mechanical properties should result from such a change in microstructure. Fine-grained deposits had been noted in the tungsten development program[3] when a batch of WF_6 containing a higher than normal vanadium impurity was used in conjunction with a glass flowmeter, resulting also in a high boron content; and in other cases when the tungsten was deposited on a molybdenum substrate. Potential doping elements will therefore include solutes such as boron, niobium, and vanadium which form stable compounds with interstitial impurities and molybdenum and tantalum. Several methods of adding the elements will be pursued.

The reaction between WF_6 and borosilicate glass flowmeter tubes had resulted in contamination of tungsten deposits with up to 1000 ppm of boron.[4] The initial doping attempts, therefore, consisted of passing the WF_6 over a glass surface maintained at 25, 100, and 200°C in successive depositions at 500°C. Boron additions achieved did not exceed 100 ppm. Metallographic examination revealed that the grain structures of all samples were columnar, and no evidence of grain refinement was found.

Fabrication of Uranium Monocarbide with Fugitive Sintering Aids

J. P. Hammond

In the last report,[5] it was pointed out that three different uranium intermetallics, UAl_2, UBe_{13}, and U_3Si_2, have proven to be very effective "eliminatable" sintering aids when using high-purity, arc-melted uranium monocarbide and intermetallics as charge materials and exercising close

---

[3]R. L. Heestand, J. I. Federer, and C. F. Leitten, Jr., Preparation and Evaluation of Vapor-Deposited Tungsten, ORNL-3662 (Aug. 1964).

[4]J. I. Federer and C. F. Leitten, Jr., Fuels and Materials Development Program Quart. Progr. Rept. June 30, 1964, ORNL-TM-920, pp. 7–10.

[5]J. P. Hammond, Fuels and Materials Development Program Quart. Progr. Rept. Sept. 30, 1964, ORNL-TM-960, pp. 10–14.

control over carbon in the uranium carbide. When using impure uranium monocarbide such as high-oxygen-containing carbide derived from UO_2 by graphitic reduction, however, only the silicide addition gave good results, that is, pellets of high density and void of secondary constituents. Densities as high as 97.0% of theoretical were reported for sintering in vacuum at 1600°C with 1.5 wt % U_3Si_2 as the addition. Beryllium vapor was provided by incorporating 0.25 wt % UBe_{13} powder within the firing crucible (external to the silicide-containing pellets) for the purpose of scavenging or cleansing the carbide powder of sinter-inhibiting contamination films. In the interim, studies have continued on the silicide addition, and some work has been done on nickel for comparison because of the acclaim it enjoys in some circles.

Table 1.4 gives the fabrication results obtained with the nickel additive using UO_2-derived uranium monocarbide. Two types of nickel were used: an ultrafine, high-purity powder prepared by the National Research Corporation by a vacuum precipitation technique and a chemical-purity-grade of nickel of −325 mesh size. The sintering temperature and amounts of nickel added compare with those reported in the literature for best results.[6]

Except for firings made with beryllium plus silicon vapors, as complementing scavenging agents, the densities obtained were disappointing. Taylor reports densities of 95% of theoretical and higher for 0.1 to 0.5 wt % Ni as the additive.[6] Figure 1.7 shows a representative microstructure for our best results, a pellet of 97.6% of theoretical achieved by sintering at 1600°C with 0.25 wt % of the ultrafine NRC nickel along with beryllium plus silicon vapors for scavenging. Pellets sintered with this additive along with the vapors at 1525°C gave comparable results (see UCNi-1, Nos. 11 and 12, Table 1.4). As is not uncommon with the nickel additive, the microstructure shows copious U_2C_3 secondary constituent (white phase). While not readily apparent in this photomicrograph, a third phase, probably U_5Ni, was also in evidence. Although

---

[6]K. M. Taylor et al., "Sintering Characteristics of UC and (U,Pu)C With and Without Small Additions of Nickel," paper presented at Symposium on Carbides in Nuclear Energy, Harwell, England, November 5–7, 1963.

Table 1.4. Fabrication Results on UO_2-Derived UC Using Nickel as Aid at 1525°C in Vacuum[a]

UCNi-1 Pellet Number[b]	Nickel Content (wt %)	Nickel Type	Vapors	Density (% TD)[c]	
				Green	Fired
1	0.02	NRC	None	62.6	86.7
2	0.02	NRC	None	62.9	86.5
3	0.1	NRC	None	62.5	89.4
4	0.1	NRC	None	62.5	89.4
5	0.25	NRC	None	62.1	90.3
6	0.25	NRC	None	62.1	90.3
7	0.25	Ordinary	None	62.5	88.5
8	0.25	Ordinary	None	62.5	88.5
9	None		None	63.4	82.5
10	None		None	63.4	82.5
11	0.25	NRC	Be,Si[d]	64.4	96.6
12	0.25	NRC	Be,Si[d]	64.5	96.5

[a] 10^{-6} torr.

[b] Pellets of 0.50-in. diam, 2 wt % camphor, 25 tsi pressing pressure; UC charge analyzed: 94.84% U, 4.74% C, 0.70% O; particle size: 5.7 μ mean.

[c] Based on theoretically dense UC.

[d] Provided from UBe_{13} and U_3Si_2 as loose powders within the tungsten-lined tantalum firing crucible.

the reactive metal vapors enabled high densification, such structures have the disadvantage of possible high-temperature weakening stemming from the secondary constituents and carbide-to-sodium carburizing effects from the sesquicarbide.

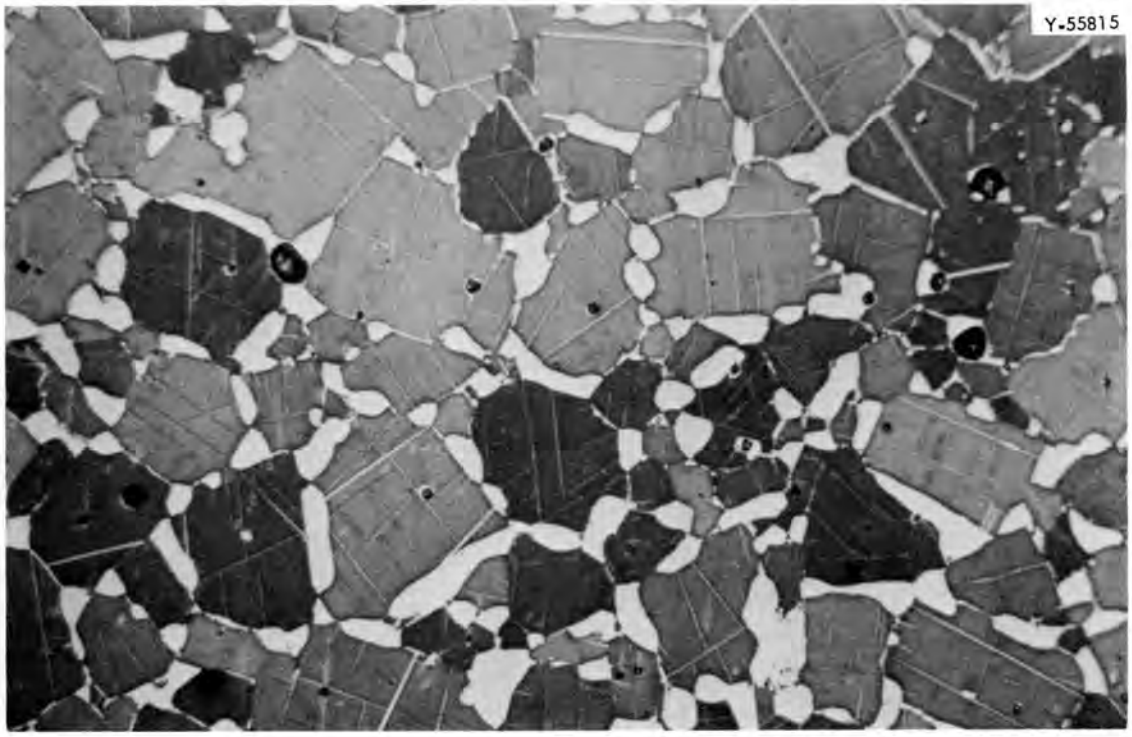

Fig. 1.7. Microstructure of UO_2-Derived UC Sintered With 0.25% NRC Nickel and Vapors of Beryllium and Silicon at 1600°C, 97.6% of Theoretical Density. Etchant: Equal parts acetic acid, H_2O, and concd HNO_3. 500×.

Table 1.5 gives the results of additional experiments conducted with silicide additives using UO_2-derived UC as charge. One-fourth weight percent UBe_{13} internally added and beryllium or beryllium-plus-silicon vapors serve as supplementary agents in sinterings conducted in vacuum at 1550°C, with crucible material as a variable. The superior densification results obtained for the series UCS-1, Nos. 9 through 14, as compared to the companion series UCS-1, Nos. 1 through 6, possibly stem from a poisoning effect produced from the graphite firing crucible used in the latter series. The graphite crucible had been baked out but not well broken in. The microstructures for the pellets sintered with beryllium-plus-silicon vapors and U_3Si_2 plus the beryllium vapor as the aids gave essentially single-phase microstructures, whereas those for the U_3Si_2-plus UBe_{13} additive showed a very small amount of an unidentified secondary phase in dispersed form. The theoretical density for the pellets fired in beryllium plus silicon vapors as the sintering aid was

Table 1.5. Fabrication Experiments on UO_2-Derived UC With Varying Aids and Crucibles at 1550°C in Vacuum[a]

UCS-1 Pellet Number[b]	Additives, wt %		Vapors[c]	Crucible	Density (% TD)[d]	
	U_3Si_2	UBe_{13}			Green	Fired
1			Be, Si	Graphite	64.5	87.4
2			Be, Si	Graphite	64.9	87.7
3	1.25		Be	Graphite	64.6	87.8
4	1.25		Be	Graphite	64.4	87.8
5	1.25	0.25		Graphite	67.0	89.9
6	1.25	0.25		Graphite	67.2	90.6
9			Be, Si	W-lined Ta	64.7	94.4
10			Be, Si	W-lined Ta	64.7	94.4
11	1.25		Be	W-lined Ta	64.1	96.0
12	1.25		Be	W-lined Ta	64.4	96.3
13	1.25	0.25		W-lined Ta	64.7	97.0
14	1.25	0.25		W-lined Ta	64.5	97.0

[a] 10^{-6} torr.

[b] Pellets of 0.50-in. diam, 2 wt % camphor, 25 tsi pressing pressure; UC charge analyzed: 94.84% U, 4.74% C, 0.70% O; particle size, 5.7 μ mean.

[c] Provided from UBe_{13} and U_3Si_2, or UBe_{13} alone as loose powders within the firing crucible.

[d] Based on theoretically dense UC.

a surprisingly high 94.4% (UCS-1, Nos. 9 and 10) and attests to the beneficial effects which stem from reactive metal vapors, even when applied to an impure grade of uranium carbide. The representative microstructure for the firings conducted with 1.25 wt % U_3Si_2 plus supplemental beryllium vapor (a highly dense, essentially single-phase structure) is shown in Fig. 1.8.

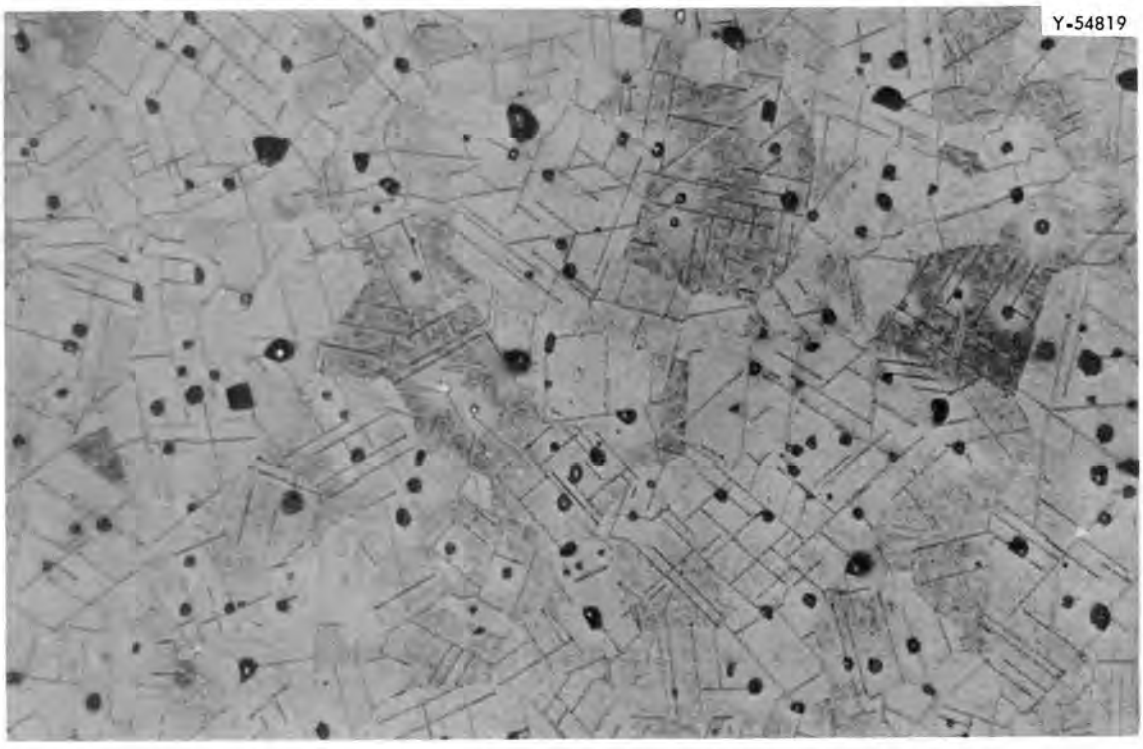

Fig. 1.8. Microstructure of UO_2-Derived UC Sintered with 1.25 wt % U_3Si_2 Plus Beryllium Vapor at 1550°C, 97.0% of Theoretical Density. Etchant: Equal parts acetic acid, H_2O, and concd HNO_3. 500X.

Experiments were conducted also with the various silicides as the additive along the lines reported last time but without the presence of beryllium as a reactive metal vapor. These are shown in Table 1.6. The data clearly show U_3Si_2 by itself to be an excellent sintering aid. These very good results suggest that silicon may possess a scavenging or cleansing effect much as do aluminum and beryllium vapors, although this was not expected from a preliminary examination of thermodynamic data. A subsequent experiment consisting of sintering straight uranium monocarbide (arc-melted grade) in the presence of silicon vapor, made available by incorporating U_3Si_2 crystals in loose form within the firing crucible (tungsten-lined tantalum), indeed gave a definite beneficial effect and revealed silicon vapor to be just as effective as aluminum or beryllium vapor in abetting the sintering of uranium carbide. A density of 92.1% of theoretical was obtained for 1550°C sintering, whereas without silicon vapor a density of only 89.6% was obtained for 1600°C sintering or 92.8% at 1900°C.

Table 1.6. Fabrication Results on UO_2-Derived UC Using Different Silicide Additives at 1600°C in Vacuum[a]

UC-22 Pellet Number[b]	Additive[c] (wt %)	Density (% TD)[d]	
		Green	Fired
18	1 1/2 U_3Si_2	67.4	97.5
19	1 1/2 U_3Si_2	67.4	97.5
20	1 1/2 USi	67.0	95.0
21	1 1/2 USi	67.4	95.0
22	3/4 Y_4Si_3	66.4	89.5
23	3/4 Y_4Si_3	66.4	89.5

[a] 10^{-6} torr.

[b] Pellets of 0.50-in. diam, 2 wt % camphor, 25 tsi pressing pressure; UC charge analyzed: 94.84% U, 4.74% C, 0.70% O; particle size 5.7 μ mean.

[c] No vapor present.

[d] Based on theoretically dense UC.

Refractory-Metal Dispersion Fuels

M. C. McIlwain J. P. Hammond

While tungsten is a potential matrix material for highly loaded refractory-metal fuel elements, especially for space applications, its use is hindered by its low-temperature brittleness. With molybdenum and chromium, this difficulty was partially overcome by the use of small additions of yttrium and the rare-earth metals[7] to scavenge harmful interstitials and possibly act as a dislocation source.[8] However, it has not

[7] E. M. Savitskii et al., Rare Earth Alloys, AEC-TR-6151, p. 257.

[8] H. Conrad, Guiding Principles for Lowering the Ductile-to-Brittle Transition Temperature in the BCC Metals, ATN-64(9236)-4 (Dec. 10, 1963).

been possible to use this approach with tungsten[9] since during melting these metals have a strong tendency to separate and sublime out. It was thought to be possible to surmount these difficulties by using some of the techniques developed in the carbide sintering studies.[10] Scouting tests to demonstrate the feasibility therefore were conducted.

To simplify handling and powder preparation, yttrium and the rare earths were added to the powder compacts as aluminides or hydrides, the aluminide powders having sufficient stability to permit handling in normal atmospheres. The hydrogen or the aluminum is removed from the compact during vacuum sintering, leaving the metals finely and uniformly dispersed through the tungsten.

The results presented in Table 1.7 demonstrate the plausibility of removing aluminum from W-YAl_2 compacts by a vacuum sintering operation while leaving the yttrium or cerium behind. In the case of sample WY-47, 98% of the aluminum was removed during sintering.

In an effort to produce highly dense samples in a form suitable for property evaluation, several rolling experiments were carried out. It was found possible to reduce small samples (5 g) of high density, such as WY-16, by picture-frame encasing with Inconel and rolling at 1000°C. However, efforts to reduce larger samples (30 g), such as WY-47 and WC-1, were unsuccessful using this technique. It is believed that insufficient side restraint was provided the larger samples by the Inconel encasement, thus causing failure during rolling. Future rolling will be carried out at 1200°C using molybdenum frames in an effort to overcome the present difficulty.

---

[9]J. F. Nachman and C. E. Lumdin, "Effect of Selected Rare Earth Additions on the Removal of Interstitials from Tungsten and Molybdenum," p. 65 in Proceedings of Conference on Research in Progress on Tungsten, ND-7777.

[10]J. P. Hammond and G. M. Adamson, Jr., "Fabrication of Uranium Monocarbide With a Volatile Sintering Temperature Depressant," paper presented at Symposium on Carbides in Nuclear Energy, Harwell, England, November 3–5, 1963.

Table 1.7. Fabrication Results of W–1 Wt % YAl_2 and W–1 Wt % $CeAl_2$

Sample	Chemical Composition, wt % (Intended) Y	Ce	Al	(By Analysis) Y	Ce	Al	Sintered Density (% TD)	Fabrication Schedule and Results
WY-16[a]	0.586		0.396	0.32		0.250	92	Cold pressed at 34,000 psi. Presintered 3 hr at 1200°C in H_2. Sintered 1 hr at 1400°C and 3 hr at 1800°C in vacuum. Rolled at 1000°C using Inconel can. Sample tended to delaminate on removal of can.
WY-37[b]	0.586		0.396	0.38		0.053	81	Cold pressed at 34,000 psi using petroleum ether-camphor binder and petroleum ether-stearic acid as die lubricant. Sintered 2 hr at 1400°C and 4 hr at 1800°C in vacuum.
WY-43[b]	0.586		0.396	0.39		0.040		Pressed at 34,000 psi using petroleum ether-stearic acid as die lubricant. Sintered 2 hr at 1430°C and 4 hr at 1800°C in vacuum.
WY-47[b]	0.586		0.396	0.35		0.008	80	Pressed at 34,000 psi using petroleum ether-stearic acid as die lubricant. Sintered 2 hr at 1430°C and 4 hr at 1800°C in vacuum. Rolled at 1000°C using Inconel can. Sample failed during rolling.

Table 1.7. (continued)

Sample	Chemical Composition, wt % (Intended) Y	Ce	Al	(By Analysis) Y	Ce	Al	Sintered Density (% TD)	Fabrication Schedule and Results
WC-1[b]		0.689	0.28		0.46	0.070	93	Pressed at 34,000 psi using petroleum ether-stearic acid as die lubricant. Sintered 2 hr at 1430°C and 4 hr at 1800°C in vacuum. Sample showed signs of melting. Rolled at 1000°C using Inconel can. Sample failed during rolling.

[a]Used Sylvania M-10 tungsten powder. Particle size, 1 μ. Oxygen content, 0.43%.

[b]Used Sylvania M-10 tungsten powder. Particle size, 1 μ. Oxygen content, 0.12%.

2. MECHANICAL PROPERTIES

J. R. Weir, Jr.

One objective of this program is to determine the effect of irradiation on the mechanical properties of alloys of interest as fuel cladding and to find a metallurgical condition for the alloys that produces the least effect of subsequent irradiation on the mechanical properties. To accomplish this, our study concerns the interaction of radiation-induced defects and the substructure of the alloys, the effect of irradiation temperature, postirradiation test variables, and neutron dosimetry in the facilities used in the irradiations. The material selected for initial study is type 304 stainless steel. The stabilized grades are also being investigated because of the effects of niobium and molybdenum on the stability of substructures formed by cold working and annealing.

Ductility of Irradiated Stainless Steel at Elevated Temperatures

W. R. Martin J. R. Weir, Jr.

The embrittlement associated with irradiated stainless steels has been shown to be an irradiation effect on the grain-boundary fracture process.[1,2] Grain size can greatly influence intergranular fracture. The effect of grain size on the nucleation and propagation of grain boundary cracks should be as given in Fig. 2.1. Decreasing the grain size increases the stress necessary to nucleate the wedge-type fracture observed for short-time tensile tests and should also lower the rate of crack propagation.

There are two methods of obtaining the different grain sizes in a material. One can cold work the material and recrystallize it at successively higher temperatures for a given length of time. This

---

[1]W. R. Martin and J. R. Weir, "Effect of Irradiation Temperature on the Postirradiation Stress-Strain Behavior of Stainless Steel," paper presented at the 67th Annual Meeting of the American Society for Testing and Materials, Chicago, Illinois, June 21–26, 1964. To be published in the proceedings.

[2]W. R. Martin, Fuels and Materials Development Program Quart. Progr. Rept. June 30, 1964, ORNL-TM-920, pp. 28–32.

ORNL DWG. 64-10128

INTERGRANULAR WEDGE TYPE FRACTURE

(a) Stress necessary for nucleation (σ_N) at the end of a sliding boundary is given by Stroh as:

$$\sigma_N = (12\mu\gamma_d/\pi L)^{1/2}$$

μ = shear modulus
γ_d = free energy where $\gamma_d = \gamma_s - \gamma_b$
L = length of sliding interface

(b) The maximum stress (σ_{max}) at the tip of a grain boundary crack has been shown by Zener to be approximately:

$$\sigma_{max} = (\sqrt{t2/L} + \sqrt{L/2t})\ \text{(applied shear stress)}$$

t = radius of curvature at the tip of the sliding region where $t \propto \gamma_s/\gamma_b$
L = length of sliding interface

if $L >> t$

$$\sigma_{max} \approx (\sqrt{L/2t})\ \text{(applied shear stress)}$$

Fig. 2.1. Equations for Predicting the Effect of Grain Size on the Fracture of Metals. Refs: A. N. Stroh, Proc. Roy. Soc. (London) Ser. A 223, 404 (1954); C. Zener, Elasticity and Anelasticity of Metals, p. 158, University of Chicago Press, 1948.

method can produce large relative differences in grain size but has the disadvantage of changing the impurity distribution and the character of the grain boundaries. A second method of producing different grain sizes is to cold work and recrystallize the material and allow grain growth to occur at one given temperature. One then varies the annealing time to produce the variation in grain size. This latter method normally does not produce large relative differences in grain size and was discarded in favor of the former method. Therefore, variation of the postworking annealing temperature was utilized. The microstructures from these treatments are given in Fig. 2.2. Martin

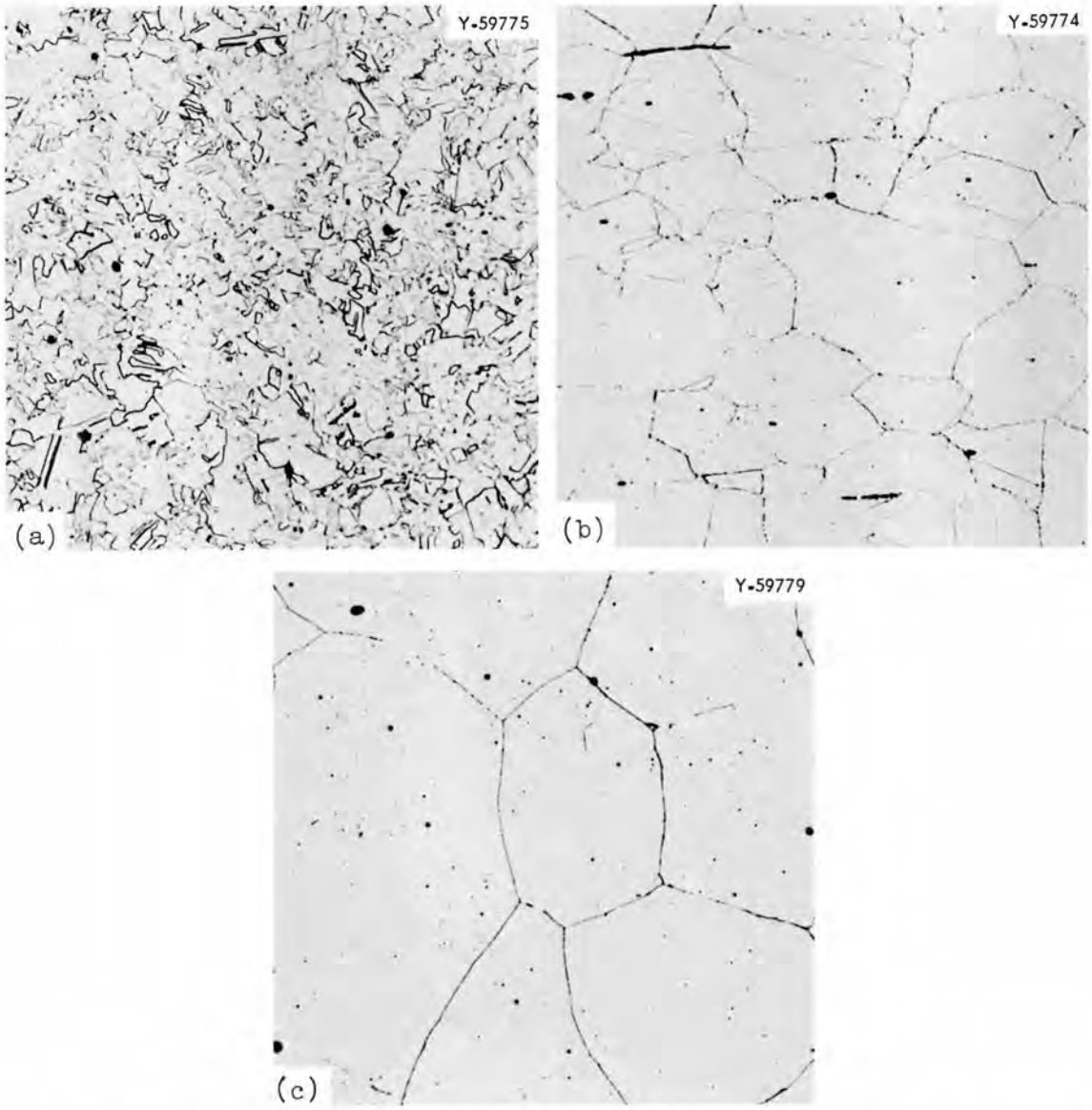

Fig. 2.2. Microstructures of Samples Given Preirradiation Anneals at (a) 926°C, (b), 1036°C, and (c) 1215°C. Etchant: $HCl-HNO_3$. 250×.

and Parker[3] have shown earlier that the cooling rate from the annealing temperature can significantly alter the ductility of materials at elevated temperature. The more rapid cooling rate produced no observable change in microstructure but increased the tendency toward grain boundary fracture. Therefore, the variable of cooling rate was selected with the rate either being that of a water quench or that of a furnace cool.

The effects of annealing temperature (grain size) and cooling rate have been investigated and these data are given in Tables 2.1 and 2.2. The ductility of the unirradiated stainless steel decreases with increasing grain size. The effect of cooling rate increases with increasing annealing temperature; the ductility decreasing with increasing cooling rate as noted earlier by Martin and Parker.[3] The effect of irradiation on the ductility of these heat-treated alloys is also given in Tables 2.1 and 2.2. The ductility of irradiated material can be significantly enhanced by decreasing the grain size.

The true ductility ($\bar{\epsilon}_f$) of materials deformed at elevated temperature is the sum of:

a. slip within a grain matrix ($\bar{\epsilon}_g$) ,

b. grain boundary shearing ($\bar{\epsilon}_b$) , and

c. widening of grain boundary cracks ($\bar{\epsilon}_c$) .

It is important to analyze the ductility of unirradiated and irradiated materials with respect to these modes of deformation. The true fracture ductility of a round rod can be determined by pre- and posttest diameter measurements. The widening of grain-boundary cracks can be estimated from photomicrographs. The slip within the matrix can be determined by the degree of grain distortion from photomicrographs using the technique of Rachinger.[4] The amount of grain boundary shearing is therefore $\bar{\epsilon}_b = \bar{\epsilon}_f - \bar{\epsilon}_c - \bar{\epsilon}_g$. Values of these terms for unirradiated and irradiated materials are given in Table 2.3. Let us first consider the

---

[3]D. L. Martin and E. R. Parker, Trans. AIME 156, 126 (1944).

[4]W. Rachinger, J. Inst. Metals 81, 33 (1952–53).

Table 2.1 Effect of Preirradiation Heat Treatment on the Ductility of Irradiated Type 304 Stainless Steel Tested at 704°C

Strain Rate (%/min)	Yield Stress (psi)		Ductility (%)				Preirradiation Annealing Temperature (°C)	Cooling Rate from Annealing Temperature	Grain Size	
			Uniform Strain		Total Elongation					
	Unirradiated	Irradiated	Unirradiated	Irradiated	Unirradiated	Irradiated			Diameter (mm)	ASTM Number
20	20.7	20.3	23.5	24.4	46.4	44.3	926	Rapid	0.012 to 0.024	8 to 10
	20.7	18.7	24.0	23.4	48.0	40.3	926	Slow	0.012 to 0.024	8 to 10
	13.6	14.2	25.6	22.4	41.2	31.2	1036	Rapid	0.064	5
	12.2	12.6	25.0	25.4	43.0	40.0	1036	Slow	0.064	5
	12.2	11.7	18.4	19.9	22.2	24.5	1215	Rapid	0.123	3
	10.0	10.2	24.9	24.5	37.0	32.4	1215	Slow	0.123	3
0.2	18.9	19.7	15.1	14.2	52.9	41.4	926	Rapid	0.012 to 0.024	8 to 10
	18.7	18.9	15.7	17.3	58.2	41.7	926	Slow	0.012 to 0.024	8 to 10
	15.3	14.8	14.3	13.7	35.2	19.1	1036	Rapid	0.064	5
	13.4	12.8	17.6	16.1	39.2	22.8	1036	Slow	0.064	5
	11.5	11.8	9.1	8.9	11.0	10.0	1215	Rapid	0.123	3
	10.4		18.6	14.9	30.3	18.8	1215	Slow	0.123	3

Table 2.2 Effect of Preirradiation Heat Treatment on the Ductility of Irradiated[a] Type 304 Stainless Steel Tested at 842°C

Strain Rate (%/min)	Yield Stress (psi		Ductility (%)				Preirradiation Annealing Temperature (°C)	Cooling Rate from Annealing Temperature	Grain Size	
			Uniform Strain		Total Elongation					
	Unirradiated	Irradiated	Unirradiated	Irradiated	Unirradiated	Irradiated			Diameter (mm)	ASTM Number
20	16.0	16.6	13.4	13.0	56.4	29.3	926	Rapid	0.012 to 0.024	8 to 10
	15.9	15.5	13.0	13.4	56.8	28.1	926	Slow	0.012 to 0.024	8 to 10
	13.8	12.6	15.8	11.7	38.8	17.7	1036	Rapid	0.064	5
	10.3	12.2	18.0	13.8	50.4	21.8	1036	Slow	0.064	5
	12.9	11.4	11.5	7.9	16.4	9.8	1215	Rapid	0.123	3
	8.7	10.9	18.1	10.9	37.0	13.5	1215	Slow	0.123	3
0.2	9.2	10.2	6.4	4.7	45.4	15.8	926	Rapid	0.012 to 0.024	8 to 10
	9.5	10.9	10.3	4.4	47.1	16.2	926	Slow	0.012 to 0.024	8 to 10
	9.5	10.7	14.8	5.7	28.0	9.7	1036	Rapid	0.064	5
	9.6	10.7	16.3	6.5	36.0	10.9	1036	Slow	0.064	5
	10.3	10.8	3.6	2.2	6.8	4.2	1215	Rapid	0.123	3
	9.2	9.4	11.2	5.0	22.5	7.8	1215	Slow	0.123	3

[a]Thermal neutron dose of 2×10^{20} neutrons/cm^2
Fast (> 1 Mev) neutron dose of 2×10^{19} neutrons/cm^2

Table 2.3. Influence of Preirradiation Heat Treatment on the Ductility of Type 304 Stainless Steel[a]

Preirradiation Heat Treatment		True Strain for Unirradiated Alloy (%)				True Strain for Irradiated Alloy (%)			
Annealing Temperature (°C)	Cooling Rate	Total Fracture	Grain Matrix	Attributable to Cracks	Grain Boundary Shearing	Total Fracture	Grain Matrix	Attributable to Cracks	Grain Boundary Shearing
926	Rapid	119	92	13	14	39	33	6	0
	Slow	129	87	8	34	41	38	3	0
1036	Rapid	47	35	8	4	26	20	2	4
	Slow	79	55	6	18	31	27	2	2
1215	Rapid	17	12	2	3	21	18	3	0
	Slow	45	18	4	23	25	18	2	5

[a]Test conditions: Deformation temperature, 842°C.
Deformation rate, 20%/min.

unirradiated material. Grain size greatly influences the magnitude of slip within the grain matrix prior to fracture. To a lesser degree, $\bar{\epsilon}_c$ and $\bar{\epsilon}_b$ are also a function of grain size. The magnitude of grain boundary shearing appears to be more dependent upon the rate of cooling from the annealing temperature. Also note that the magnitude of grain-boundary shearing relative to the total ductility increases with increasing grain size.

Similar effects are noted for the irradiated materials except that the irradiated materials fracture at a strain for which no grain boundary shearing is observed, suggesting that grain-boundary shearing is restricted in irradiated alloys.

The effect of irradiation on the ductility of stainless steel as a function of annealing temperature is shown in Fig. 2.3. Note that the ratio of irradiated to unirradiated ductility (as given by total elongation) decreases with increasing annealing temperature except for preirradiation annealing temperatures in the range of 1215°C. The irradiation effects appear to saturate for samples slowly cooled but decrease for specimens rapidly cooled from 1215°C. There are two possible explanations.

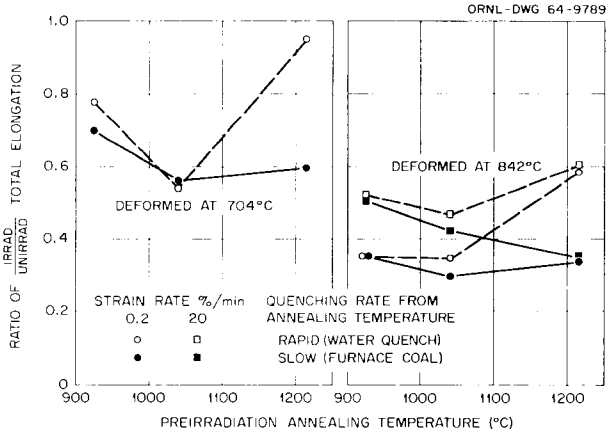

Fig. 2.3. Influence of Preirradiation Heat Treatment on the Elevated Temperature Irradiation Embrittlement of Stainless Steel.

Unirradiated samples rapidly cooled from 1215°C do not exhibit marked grain-boundary shearing, as shown in Table 2.3. Since one of the irradiation effects is to restrict grain-boundary sliding, these heat treated alloys are least affected. A second explanation is that impurities tend to desegregate[5] at the higher annealing temperatures and a rapid quench prevents the segregation of these elements, such as boron to the grain boundaries. Thus, upon irradiation the concentration of boron available at the grain boundary for transmutation to helium is greatly reduced. Therefore, the concentration of helium at the boundary is reduced and consequently the magnitude of the irradiation embrittlement is reduced. Both of these explanations appear to be plausible. Speculation of the latter concerns the degree of desegregation[6,7,8] of interstituals from the boundary at elevated temperature.

Ductility of Irradiated Metals (Copper, Nickel, and Iron) at Elevated Temperatures

W. R. Martin

Radiation-induced embrittlement of complex structural materials has been noted at conditions for which intergranular fracture is observed. Presently, it is believed that the embrittlement is associated with helium atoms and/or bubbles that affect the nucleation and propagation of grain boundary cracks. But the mechanism of embrittlement in complex

---

[5]D. McLean, Grain Boundaries in Metals, p. 336, Clarendon Press, Oxford, England, 1957.

[6]C. Crussard, J. Plateau, and G. Henry, "Influence of Boron in Austenitic Alloys," pp. 1–91 in Joint International Conference on Creep, Institute of Mechanical Engineers, London, England, 1963.

[7]M. Hoch, The Problem of Grain Boundary Segregation of Boron in Iron- and Nickel-Base Alloys, NMPO-TM-64-7-11 (1964).

[8]L. Colombier, J. Hochmann, and J. Bourrat, Compt. Rend. 245, 1135 (1957).

alloys is complicated by precipitation phenomena which may or may not be important to the mechanism of irradiation embrittlement. To investigate the importance of precipitation, relatively pure metals were irradiated to determine if an irradiation-induced elevated-temperature ductility effect exists. The metals – copper (99.993%), Nickel-270, and electrolytic iron (99.97%) – were irradiated to a thermal neutron dose level of 7×10^{20} neutrons/cm^2. For these data, total elongation and uniform strain were used as a measure of ductility. The irradiation effect is represented as the ratio of irradiated to unirradiated ductility as a function of deformation temperature. These curves for copper, nickel, and iron are given in Fig. 2.4. It is noted that the general aspects of the ductility effect are the same as noted for stainless steel and reported earlier.[9] It is believed[10] that the low-temperature effect (Region 1) is associated with fast neutron damage. The irradiation-induced defects result in a structure that has a high flow stress and low work hardening coefficient. The low hardening coefficient results in a low uniform elongation and, as a consequence, a reduction in total elongation.

The effect at elevated temperature (Region 2) is not reversible by annealing at the usual solution annealing temperature as earlier demonstrated for Hastelloy N (ref. 11) and stainless steel.[12] The cause of the embrittlement at elevated temperature is believed to be due to helium. The helium is present as a result of the transmutation of boron (ref. 10), the (n,α) reaction. The boron content as determined[13]

---

[9]W. R. Martin and J. R. Weir, Effect of Irradiation Temperature on the Postirradiation Stress-Strain Behavior of Stainless Steel, ORNL-TM-906 (Oct. 1964).

[10]W. R. Martin and J. R. Weir, "Effect of Preirradiation Heat Treatment on the Postirradiation Ductility of Irradiated Stainless Steel," paper presented at the 1964 Annual Meeting of the American Nuclear Society, San Francisco, Calif., Nov. 30–Dec. 3, 1964. To be published in Nuclear Applications.

[11]W. R. Martin and J. R. Weir, "Effect of Elevated Temperature Irradiation on Hastelloy N," to be published in Nuclear Applications.

[12]W. R. Martin and J. R. Weir, Nature 202(4936), 997 (1964).

[13]J. C. Franklin and W. D. Harmon, Spark Source Mass Spectrograph, Y-KG-24 (Oct. 1, 1964).

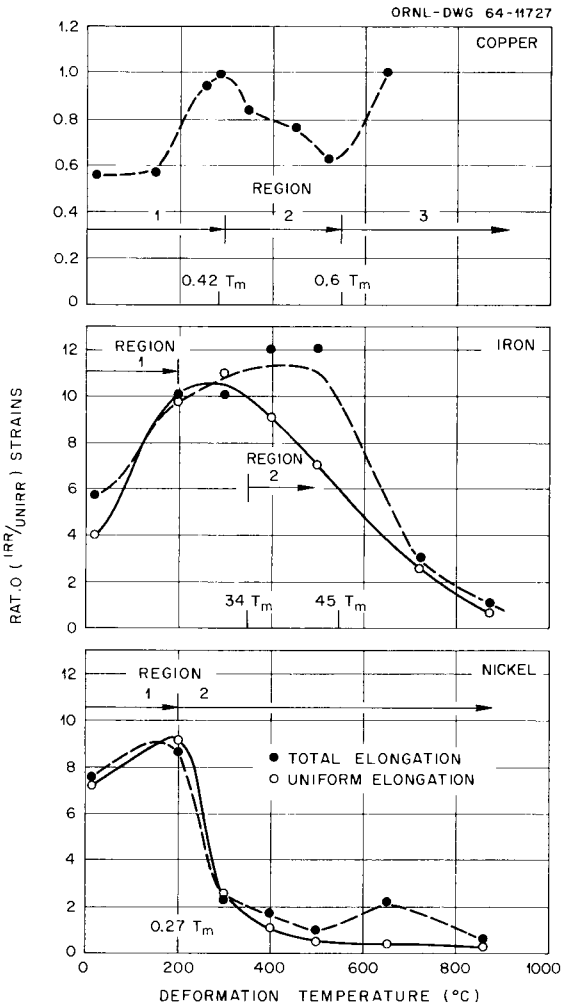

Fig. 2.4. Effect of Irradiation on the Ductility of Pure Metals.

by the spark source mass spectrograph for copper, nickel, and iron are 45, 390, and 500 ppb, respectively. The atom fraction of helium if distributed homogeneously would be in the range of 10^{-8} to 10^{-7}. Since radiation-induced embrittlement occurs in these relatively pure metals at elevated temperature, it appears that radiation effects of precipitation of compounds in complex alloys is not the primary mechanism for the damage to ductility. The elevated-temperature embrittlement of copper, however, appears to be limited to a narrow temperature range, 450 to 550°C. Above 550°C (Region 3) the copper is not affected. Typical fractures of copper, nickel, and iron in this temperature range ($\sim 0.67\ T_m$) are shown in Fig. 2.5. The fractures of the iron and nickel for which the embrittlement at elevated temperature is observed are

Fig. 2.5. Photograph of Copper, Nickel, and Iron Fractured in Air at Approximately 0.67 T_m at a Strain Rate of 0.2%/min.

intergranular. The fractures in the copper appear to be transgranular although much recrystallization, grain-boundary shearing, and grain growth have occurred in the specimen. Figure 2.6 illustrates the microstructure of the copper at fracture for 107, 250, and 550°C. Note the grain growth in the specimen tested at 550°C. The upper limit for the elevated-temperature embrittlement for copper may be due to one of the following. The concentration of helium is at least an order of magnitude lower than that in the iron and nickel. Wedge-type grain-boundary fracture is believed to be the consequence of grain-boundary shearing, either as a mode of deformation itself or as that accommodating slip within the grain matrix. The grain-boundary shearing results in stress concentrations at the junction of other subgrain and major boundaries

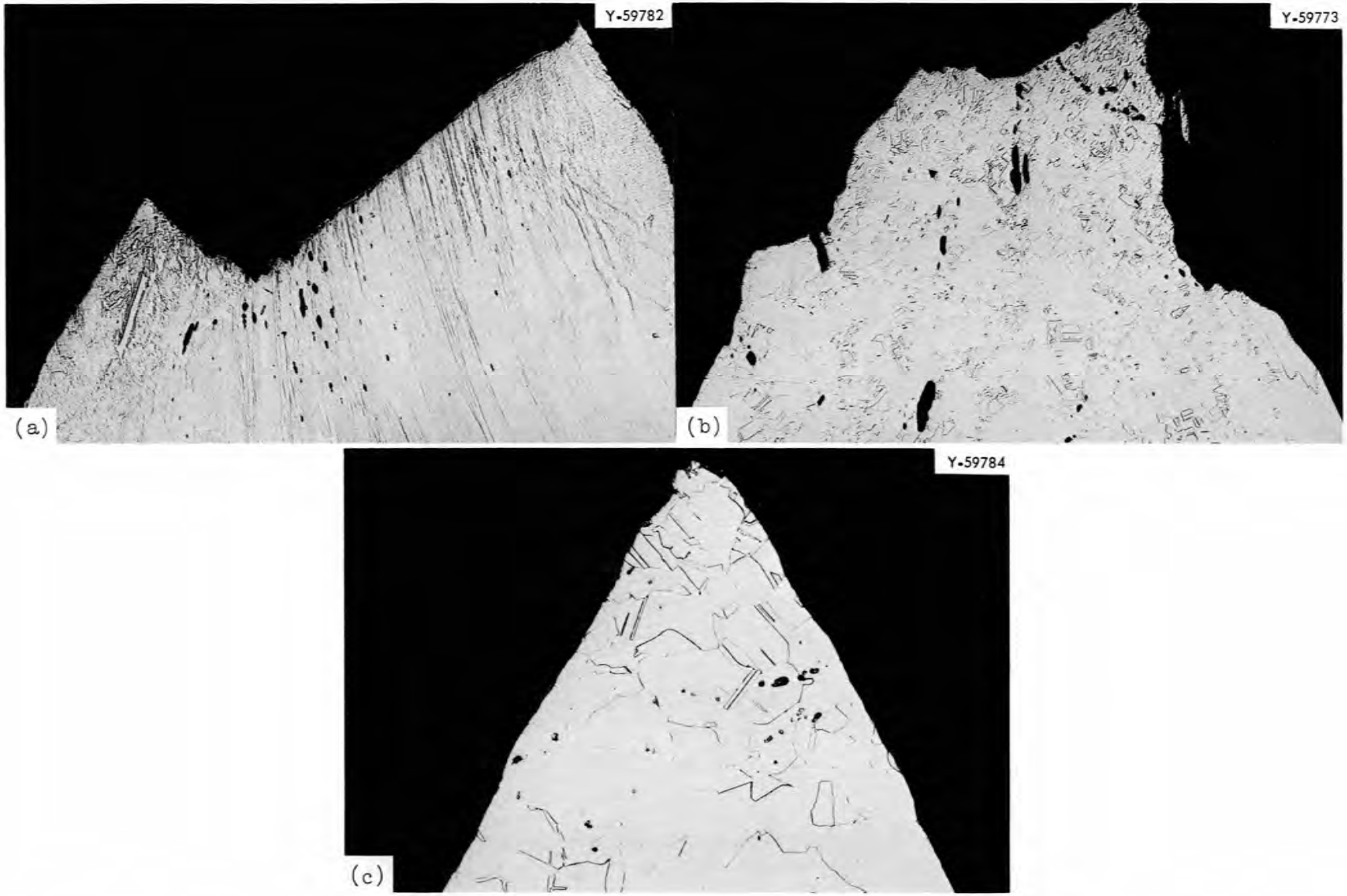

Fig. 2.6. Photomicrographs of Unirradiated Copper Deformed at (a) 107, (b) 250, and (c) 550°C. 100×.

(i.e., jogs, subgrain boundaries and triple points). If these stresses are not relieved by relaxation within the grain or by grain-boundary migration, the result is the initiation of a grain-boundary crack. Therefore, in a high-purity material with a low helium concentration, it is possible that the stresses accompanying the grain-boundary shearing are relieved by both grain-boundary migration and fold formation at the triple points. These processes would be dependent [14,15] upon the impurity content of the metal and the temperature of testing. It might be expected that a similar effect would be observed for nickel and iron at higher deformation temperatures for tests performed in a noncontaminating environment (i.e., vacuum). Rhines and Wray[16] have observed an improvement in the ductility of brass and Monel metal at an elevated temperature that corresponds to rapid grain growth. Chen and Machlin[17] found a similar effect for copper when testing in vacuum and air at 700°C. Also it is known that aluminum and its alloys fracture intergranularly over a narrow temperature range[18,19,20] which perhaps is a reflection of high mobility of grain boundaries in this metal at elevated temperatures. It has also been demonstrated that helium, introduced by the cyclotron, can affect the recrystallization and grain growth of aluminum. Thus, the low ductility observed for alloys fracturing intergranularly (i.e., low strain rates at elevated temperatures) is a grain-boundary effect. This effect is related to fracture at strains for which no grain-boundary shearing is observed and the effect can be negated by grain-boundary migration.

---

[14]B. J. Neild and A. G. Quarrel, J. Inst. Metals 85, 490 (1957).

[15]P. N. Davies and B. Wilshire, Trans. Met. Soc. AIME 221, 1265 (1961).

[16]F. N. Rhines and P. J. Wray, Am. Soc. Metals Trans. Quart. 54, 117 (1961).

[17]C. W. Chen and E. S. Macklin, Trans. Met. Soc. AIME 218, 177 (1960).

[18]A. Mullendore and N. J. Grant, Trans. AIME J. Metals 6, 973 (1954).

[19]G. Gemmell and N. J. Grant, Trans. AIME J. Metals 9, 417 (1957).

[20]J. McKeown, R. Eborall, and R. D. S. Bushey, Metallurgica 50, 13 (1954).

Substructure Studies

H. E. McCoy

The initiation of a program to correlate radiation effects with substructure has been discussed previously.[21] Sheet specimens 0.010 in. thick of types 304, 302 and 316 stainless steel have been irradiated and tested at room temperature. The irradiation temperature was 45°C and the neutron dose was 8×10^{19} neutrons/cm^2 thermal and 4×10^{18} neutrons/cm^2 fast (> 2.9 Mev). The type 304 stainless steel was evaluated in three conditions:

1. annealed 1 hr at 1040°C,
2. annealed 1 hr at 1040°C, cold worked 10%, annealed 24 hr at 480°C, and annealed 100 hr at 705°C, and
3. same as treatment 2 except cold worked 20%.

The type 302 stainless steel was evaluated in the as-annealed condition (1 hr at 1200°C) and after having received treatment 3. The type 316 stainless steel was evaluated in the as-annealed condition (1 hr at 1090°C) and after having received treatment 3. Specimens were given postirradiation anneals of 1 hr at 400, 800, and 1200°C to determine the influence of structure on the kinetics of the annealing of irradiation damage. All tests were carried out at room temperature at a strain rate of 0.025 min.$^{-1}$. Although the results have not been fully analyzed, the data given in Table 2.5 illustrate several important features of these tests. The data show consistently that the ratio of the yield stress of the irradiated material to that of the unirradiated material is greater for the solution-annealed material and decreases as the amount of cold working increases. This is according to expectation. The data also show consistently that this ratio approaches unity or less when the material is given a postirradiation anneal of 1 hr at 1200°C. The data also show that for treatment 1 the ratio in the as-irradiated condition is highest for types 302 and 316 stainless steel and considerably less for type 304

---

[21] H. E. McCoy, Quarterly Progress Report: Irradiation Effects on Reactor Structural Materials, February, March, April 1964, HW-82379, p. 10.1.

Table 2.5. Tensile Properties of Several Stainless Steels at Room Temperature

Type Stainless Steel	Treatment[a]	Postirradiation Anneal[b] (°C)	Ratio of Yield Stress	Ratio of Uniform Elongation
			Irradiated to Unirradiated	Irradiated to Unirradiated
304	1	None	1.75	0.84
304	2	None	1.38	0.37
304	3	None	1.25	0.74
304	1	1200	0.86	1.9
304	2	1200	0.80	2.0
304	3	1200	0.83	2.1
302	1	None	2.10	0.635
302	3	None	1.63	0.780
302	1	1200	0.855	1.37
302	3	1200	1.02	1.35
316	1	None	2.03	0.665
316	3	None	1.08	0.520
316	1	1200	0.975	1.46
316	3	1200	0.855	1.77

[a]Treatment 1: solution anneal.

Treatment 2: solution anneal, 10% cold work, 24-hr anneal at 482°C, and 100-hr anneal at 704°C.

Treatment 3: solution anneal, 20% cold work, 24-hr anneal at 482°C, and 100-hr anneal at 704°C.

[b]One-hour duration.

stainless steel. For the material given treatment 3, type 302 stainless steel shows the largest increase in yield strength ratio, type 304 stainless steel is considerably smaller and type 316 stainless steel is practically unchanged.

The elongation figures do not seem as consistent. The ratio of the uniform elongation of the irradiated material to that of the unirradiated material is about 0.6 for types 302 and 316 stainless steel and about 0.8

for type 304 stainless steel having treatment 1. Treatment 2 produces a very low ratio for type 304 stainless steel. Treatment 3 produces lower ratios than treatment 1 for types 304 and 316 stainless steel and a higher ratio for type 302 stainless steel. A postirradiation anneal of 1 hr at 1200°C increases the ductility ratio to greater than unity.

Although these tests indicate that forming a substructure does not significantly improve the uniform elongation at room temperature, it should be pointed out that the dose these specimens were subjected to was not very high and the minimum uniform elongation observed was 13%. Higher doses may produce a different picture. It is also possible that the ductility minimum[22] in stainless steel might be lessened by the presence of a substructure. These possibilities will be considered as this work continues.

---

[22]W. R. Martin, Fuels and Materials Development Program Quart. Progr. Rept. June 30, 1964, ORNL-TM-920, p. 30.

3. NONDESTRUCTIVE TEST DEVELOPMENT

R. W. McClung

Our program is intended to develop new and improved methods of evaluating reactor materials and components. To achieve this we are studying various physical phenomena, developing instrumentation and other equipment, devising application techniques, and designing and fabricating reference standards. Among the methods being actively pursued are electromagnetics (with major emphasis on eddy currents), ultrasonics, and penetrating radiation. In addition to our programs oriented toward the development of methods, we are studying these and other methods for evaluation of problem materials and developing techniques for remote inspection.

Electromagnetic Test Methods

C. V. Dodd

We have continued research and development on electromagnetic phenomena on both an analytical and an empirical basis. As part of the program, we are studying the mathematical determination of impedance of an eddy-current coil and other electromagnetic field parameters as a function of coil dimensions, frequency, specimen conductivity and permeability, and coil-to-specimen spacing or "liftoff." The relaxation techniques allow the solution of the electromagnetic boundary value problem on a digital computer. The differential equations for the field are approximated by finite difference terms. By making a number of correcting calculations, the values of the field can be made to converge to agreement with the differential equation at every point. The program has been applied to the problem of a coil encircling a ferromagnetic rod with a relative permeability of 200. Figure 3.1 shows a cross section of the rod and coil with equipotential contours of the field. Note the lack of penetration of the field into the rod and the sharp decrease of the field intensity. The contours inside the rod are proportional to the actual eddy-current flow inside the rod. The shaping of this current flow with ferrite will also be studied.

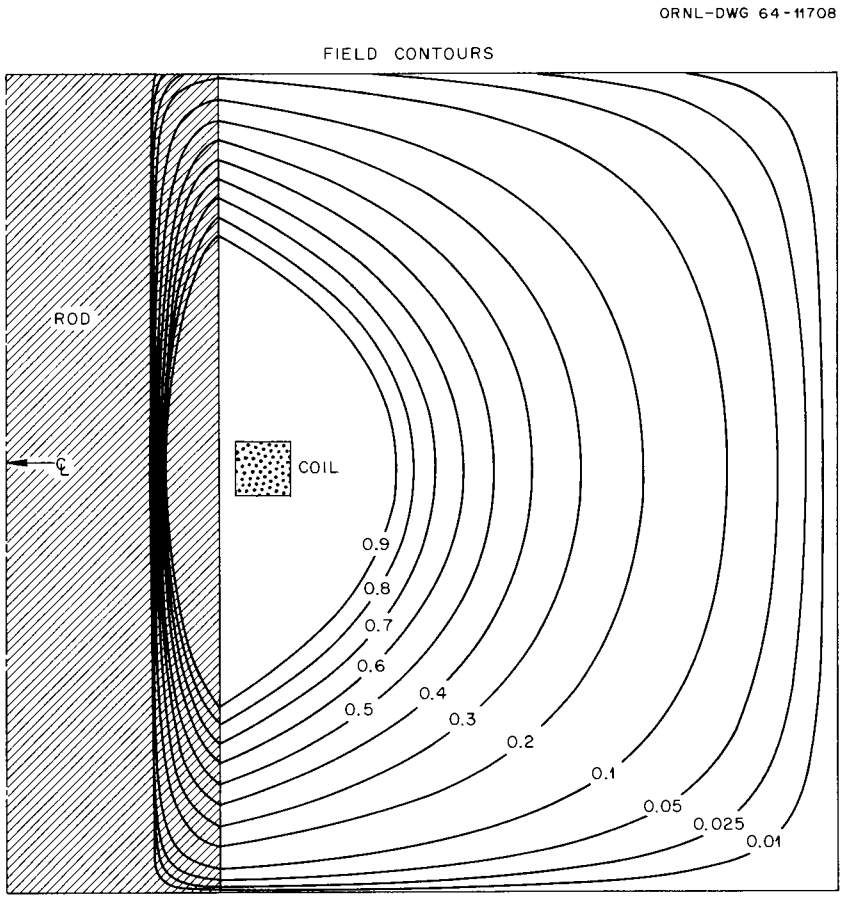

Fig. 3.1. Equipotential Contours of the Magnetic Field in a Ferromagnetic Rod Inside an Encircling Coil.

We are continuing development on the phase-sensitive eddy-current instrument. A vibrating probe has been assembled and tested with the phase-sensitive instrument. There was considerable increase in the sensitivity to defects, but it was not as good as the present mechanical inspection systems. Refinements will be made in the probe to increase this sensitivity.

Ultrasonic Test Methods

K. V. Cook

We are continuing to work on the problems encountered in tubing inspection. A major problem is the establishment of realistic ultrasonic notch standards for calibration. Since electrical discharge

machining appears to be a reliable method for making both inner- and outer-surface notches, we have purchased a laboratory-model electrical-discharge machine. Preliminary work has been done with this machine on Inconel "X" and Mo—0.5% Ti alloys. Figure 3.2 shows a typical curve of tool feed vs notch depth generated on Mo—0.5% Ti. To date we have been very successful in cutting reproducible notches on tubing outer surfaces; however, we are encountering difficulties with inner notches in small-diameter tubing (inner diameters less than 0.350 in.). Thus far, we have demonstrated that we can fabricate notches 1/8 in. long, 0.001 in. deep, and approximately 0.002 in. wide in Inconel "X" material. Further work is planned on different materials so that ratios of tool feed vs notch depth can be established. Also we hope to decrease the width of our notches and make them more realistic.

We are also concerned with the accurate measurement of the reference notch depth. One way in which we have been determining depths is to use differential focusing techniques with a microscope. On outer-surface notches we simply focus on the bottom of the notch and on top of the tube and then the difference in the lens position is the notch depth. However, with inner-surface notches this technique is impossible unless the tube is split. Hence, for inner-surface notches we have developed techniques for casting rubber replicas of the defects and then measuring their depths by the differential focusing technique. We have been successful in replicating inner-surface notches as far as 3 in. from the end of tubes with an inner diameter as small as 0.230 in. A silicon rubber (RTV-60) is used for these castings on both inner- and outer-surface notches. We have found that thinning the rubber mix with toluene improves its pouring characteristics and practicality of use in areas of poor accessibility. No loss in accuracy has been noted with this addition. Metallographic sections of both notches and their replicas have been taken and correlation between the two are excellent. Figure 3.3 shows, in cross section, an approximate center position of a 1/8-in.-long, 0.001-in.-deep, 0.0025-in.-wide outer-surface notch in Inconel "X" tubing. The differential focusing technique was used to measure the depth of this notch before sectioning. The apparent depth

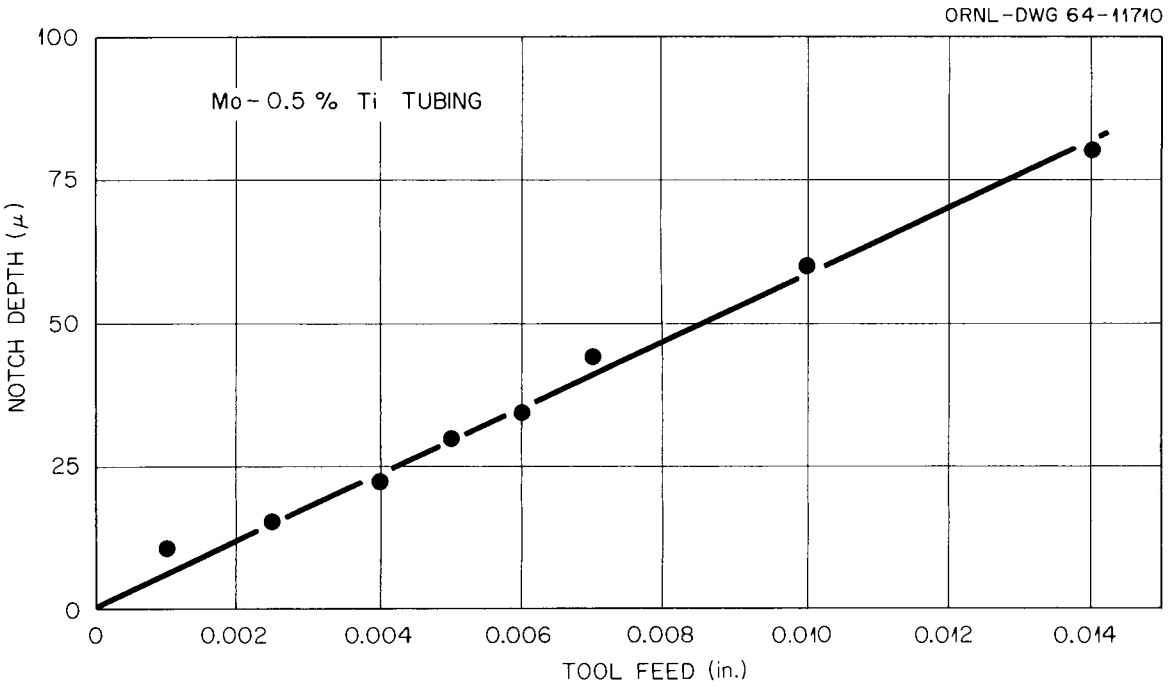

Fig. 3.2. Calibration Curve for Machining of Notches in Mo–0.5% Ti Tubing.

as measured by this technique was (0.00100 ± 0.00008) in. as evident from the photomicrograph, the depth was confirmed. Figure 3.4 is a cross section of a replica of a machined notch.

Penetrating Radiation

Gamma Scintillation Gaging – B. E. Foster, S. D. Snyder

Fuel-Rod Scanner. We are continuing the application of x- and gamma-ray attenuation to the evaluation of fuel elements. Variation in transmitted intensity can be monitored readily by scintillation gaging and can be related through proper calibration to the fuel loading homogeneity within the area of the radiation beam. We have recently designed and fabricated a scanner for the investigation of fuel homogeneity in fuel rods. The scanner is shown in Fig. 3.5. Rods with outside diameter

Fig. 3.3. Metallographic Cross Section of an 0.001-in. Deep Electro-discharge-Machined Notch in Inconel "X" Tubing. As polished. 500X.

Fig. 3.4. Cross Section of a Rubber Replica of a Machined Outer-Surface Notch. 500X.

Fig. 3.5. Scanner Used to Determine the Fuel Homogeneity in Fuel Rods.

from 0.250 to 0.750 in. can be moved longitudinally through collimated radiation beams at speeds of 2, 4, 8, 16, and 24 in./min. The maximum scan length is 5 ft, but a 10-ft rod can be scanned by turning the rod end-for-end after one-half has been scanned. The minimum length of scan is 6 in. The various scan speeds are obtained through a rack and pinion drive system with a Slo-Syn motor driver and a series of interchangeable pinion gears.

We have equipped the scanner with two radiation sources, 2 curies of cobalt-60 and 5 curies of cesium-137, housed in a single container with approximately 6 in. of lead separating the two sources. Also, we have provided versatility of the beam collimation by having six different

lead collimators with rectangular openings, as follows: (1) 1/16 × 3/16 in., (2) 1/16 × 1/4 in., (3) 1/16 × 1/2 in., (4) 1/8 × 1/8 in., (5) 1/8 × 1/4 in., and (6) 1/8 × 1/2 in. The rod centering and guide rollers are an integral part of each collimator assembly to assure good alignment of rod diameter with collimator center line. Collimator support plates that slide out of the irradiation beam allow for easy and safe interchange of collimators. The detectors, each a NaI (Tl) crystal optically coupled to a photomultiplier are housed above each collimator and are accessible from the back of the housing.

With this system we shall be able to optimize the source, collimator size, and scanning speed as related to rod diameter for fuel homogeneity inspection.

Photomultiplier Calibration System. Specifications on fuel distribution within an element are becoming more stringent. The area of interest for fuel homogeneity in a fuel plate has been less than 0.005 $in.^2$ in some instances. This small spot size interrogation requires rapid scanning speeds to minimize the inspection time per fuel element. These requirements thus place a severe burden on the radiation detector and associated circuitry. It is necessary that the detector be designed for optimum operation with little deviation.

To assure ourselves that the detectors are operating properly, we designed and fabricated a photomultiplier calibration chamber and assembled it with a single channel analyzer as shown in Fig. 3.6. With this system we can "tune" the detectors for optimum operation and, through routine observations, note any deterioration of the detector system.

The system consists of a standard single channel analyzer and cadmium–copper-lined lead-shielded chamber. The radiation detector is a NaI (Tl) crystal optically coupled to a photomultiplier tube. A voltage output of the photomultiplier tube is defined as the pulse height. The height of each pulse from the crystal-photomultiplier and amplifier combination is proportional to the amount of incident gamma-ray energy dissipated by the detector. These small voltage pulses from the detector are fed through a preamplifier to a linear amplifier and pulse-height analyzer for shaping and selection between two definite voltage levels.

Fig. 3.6. System for Optimum Calibration of Photomultiplier Tubes for Gamma Scintillation.

The output from the pulse-height analyzer then goes to a linear count-rate meter and finally to a recorder. Also a decade scaler and timer are included which allows the operator to determine the count rate at any point within the gamma spectrum for any time period up to 10^6 sec.

A photomultiplier divider network has been constructed and installed in the lead chamber. The features of the divider network include potentiometers for adjusting the accelerating and focusing potentials of individual photomultiplier tubes. These potentials are measured with electrostatic voltmeters. After the potentials are determined for optimum operation of the photomultiplier tube, the resistance values can be determined for fabrication of the permanent divider network for that particular detector.

X-Ray Imaging with Closed-Circuit Television – W. H. Bridges

The use of an x-ray sensitive closed-circuit television has been described previously.[1,2] The images obtained in that work were essentially black and white. The use of such a system for radiographic inspection, however, places a demand for "grey." We are currently engaged in determining the minimum contrast that we can ascertain with our present system.

Closed-circuit television for radiographic inspection has the primary advantage of the immediacy of the information. To be useful, however, the sensitivity to radiation must be good enough to detect the small changes resulting from a defect in the material under study. The operating voltages applied to the x-ray sensitive vidicon may be adjusted to give extremely good sensitivity, but an extremely poor image. Figure 3.7 illustrates the response of a beryllium window vidicon to 100-kvcp x rays without regard to image quality. The change in slope to negative values for the −50 beam volt curve is the result of a rapidly increasing background current and a saturation value is reached. When this occurs, the image is no longer useful.

In order to establish the "defect sensitivity," a rather unusual penetrameter has been made. It is about 7 1/2 in. in diameter and 30 mils thick. There are indentations in it ranging from 1-mil diam and 1 mil deep to 20-mil diam and 20 mil deep. The holes with varying diameters are arranged concentrically and those with varying depths go from near the center to close to the periphery. The circular hole pattern was chosen so that the specimen can be easily rotated while watching the telemonitor. The motion makes the "defect" easier to see, and also the smallest indentation that can be seen is relatively easy to locate. In this way, we shall be able to establish proper operating conditions for many varieties of radiographic inspection.

---

[1]W. H. Bridges, Fuels and Materials Development Program Quart. Progr. Rept., June 30, 1964, ORNL-TM-920, pp. 44–46.

[2]W. H. Bridges, Fuels and Materials Development Program Quart. Progr. Rept. Sept. 30, 1964, ORNL-TM-960, p. 21

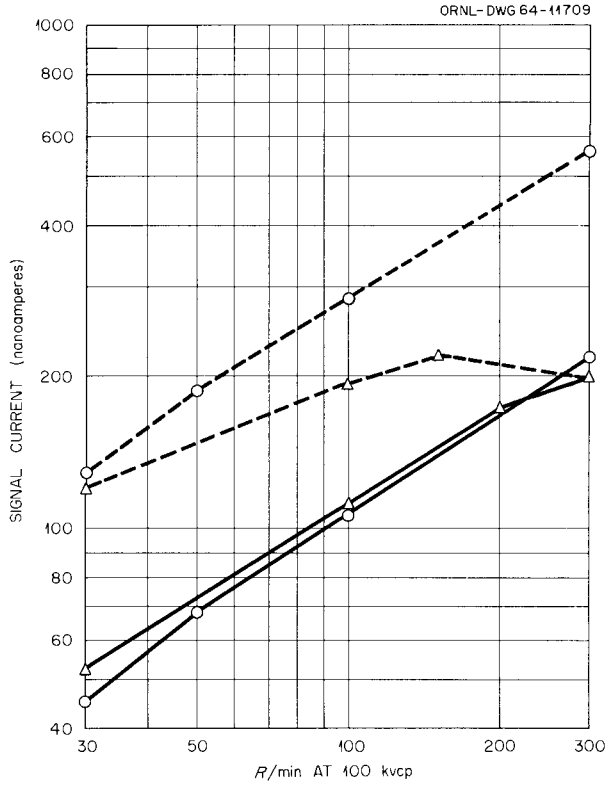

Fig. 3.7. Response of X-Ray Sensitive Vidicon as a Function of Varying Beam and Target Voltages.

Inspection Development of Problem Materials

K. V. Cook R. W. McClung

We have continued to work on nondestructive tests for unusual materials that are difficult to inspect and on new materials that have no evaluation history. This has included such items as graphite and refractory metals including nickel-, tungsten-, tantalum-, and niobium-base alloys. We found that conventional penetrant, radiographic, and ultrasonic techniques could be applied to T-111 and B-66 alloy tubing.[3]

[3]K. V. Cook and R. W. McClung, Nondestructive Evaluation of T-111 and B-66 Alloy Tubing, ORNL-TM-990 (Dec. 1964).

4. SOLID REACTION STUDIES

T. S. Lundy

Our purpose is to provide information concerning solid-state reactions of importance in the development of materials for high-temperature application. We are emphasizing the study of mechanisms of these reactions by measuring diffusion rates in the solid state by various methods. In particular, we are studying the diffusion rates in various body-centered cubic refractory metals over wide ranges of temperatures.

During this quarter, we have concentrated on measuring the volume diffusion coefficients of ^{95}Nb and ^{182}Ta in niobium over the temperature range 878 to 2400°C. This work is covered in a paper to be published in the open literature and included here as our contribution to this report.

Diffusion of ^{95}Nb and ^{182}Ta in Niobium[1]

T. S. Lundy F. R. Winslow R. E. Pawel
C. J. McHargue

Introduction

Previously reported studies of self-diffusion in niobium were by Resnick and Castleman[2] and Peart, Graham, and Tomlin.[3] The data of Resnick and Castleman over a temperature range 1585 to 2120°C show considerable scatter but can be represented by

$$D = (12.4 \pm 0.8) \exp [-(105{,}000 \pm 3000)/RT] \text{ cm}^2/\text{sec} . \quad (1)$$

The limited data of Peart, Graham, and Tomlin follow the equation

$$D = 1.3 \exp (-95{,}000/RT) \text{ cm}^2/\text{sec} . \quad (2)$$

In view of recent diffusion data for β-zirconium (ref. 4) and β-titanium (ref. 5) in which Arrhenius-type plots do not yield straight

---

[1]Submitted to Transactions of the Metallurgical Society of AIME.

[2]R. Resnick and L. S. Castleman, Trans. Met. Soc. AIME 218, 307 (1960).

[3]R. F. Peart, D. Graham, and D. H. Tomlin, Acta Met. 10, 519 (1962).

[4]J. I. Federer and T. S. Lundy, Trans. Met. Soc. AIME 227, 592 (1963).

[5]J. F. Murdock, T. S. Lundy, and E. E. Stansbury, Acta Met. 12, 1033 (1964).

lines and of the potential high-temperature uses of niobium and its alloys, we thought it important to investigate the diffusion behavior of this body-centered cubic refractory metal over a large temperature range. This has recently been done for molybdenum,[6] chromium,[7] vanadium,[8,9] and tantalum.[10] Niobium was a particularly suitable material for this study largely because of the development of an anodizing and stripping sectioning technique which enables diffusivities as small as 10^{-19} cm^2/sec to be determined accurately.[11] In addition to self-diffusion data, data were obtained for the diffusion of ^{182}Ta in niobium and for the effect of varying oxygen content on self-diffusion.

Experimental Procedure

Materials. – The niobium was obtained from three sources: (1) melting stock from Shieldalloy Corporation, (2) electron-beam melted single crystals, 1/2 in. in diameter, from Semi-Elements, Inc., and (3) oxygen-doped, electron-beam melted single crystals from Materials Research Corporation. The melting stock was electron-beam melted and specimens 5/8 in. in diameter and 1/2 in. long were machined from the center of the bar. The analysis supplied by the vendor and an interstitial analysis of one of the specimens are given in Table 4.1. The single

---

[6]J. Askill and D. H. Tomlin, Phil. Mag. 8, 997 (1963).

[7]J. Askill, "Tracer Diffusion Studies in Molybdenum," paper presented at the International Conference on Diffusion in Body Centered Cubic Materials held at Gatlinburg, Tennessee, September 16–18, 1964. Proceedings to be published.

[8]R. F. Peart, "Vanadium Self-Diffusion," paper presented at the International Conference on Diffusion in Body Centered Cubic Materials held at Gatlinburg, Tennessee, September 16–18, 1964. Proceedings to be published.

[9]T. S. Lundy and C. J. McHargue, "Diffusion of V^{48} in Vanadium," to be published in Transactions of the Metallurgical Society of AIME.

[10]R. E. Pawel and T. S. Lundy, "The Diffusion of Nb^{95} and Ta^{182} in Tantalum," submitted to Acta Metallurgica for publication.

[11]R. E. Pawel and T. S. Lundy, J. Appl. Phys. 35, 435 (1964).

Table 4.1. Major Impurity Content of Niobium Polycrystals.

Element	Vendor Analysis (ppm)	ORNL Analysis[a] (ppm)
Tantalum	1200	ND
Titanium	100	ND
Iron	300	ND
Tungsten	400	ND
Carbon	100	50
Nitrogen	100	79
Oxygen	200	63
Hydrogen	15	13

[a]ND – not determined.

crystals (type 2 above) were cut with a jeweler's saw to specimens about 3/8 in. long. The interstitial analysis of these crystals is given below:

Element	Content, ppm
Carbon	20
Nitrogen	14
Oxygen	100
Hydrogen	2

This material was used for most diffusion anneals below 1900°C; exceptions are noted in the results. The interstitial analysis of the oxygen-doped crystals (type 3 above) is given in Table 4.2.

Table 4.2. Interstitial Analysis of Oxygen-Doped Niobium Single Crystals

Element	Rod I Content (ppm)	Rod II Content (ppm)
Nitrogen	15	20
Oxygen	250	420
Hydrogen	3	7

The isotopes ^{95}Nb and ^{182}Ta were obtained from the Isotopes Division, Oak Ridge National Laboratory, in the form of oxalate solutions. Niobium-95 decays with a half-life of 35 days by the emission of a 0.76 Mev gamma. This isotope was contaminated with less than 0.02% ^{95}Zr and less than 0.1% ^{103}Ru. Tantalum-182 decays with a half-life of 112 days by the emission of 1.1 and 1.2 Mev gammas.

Specimen Preparation. – Polycrystalline specimens for high-temperature anneals were machined and then alternately abraded and etched several times in 80% HNO_3–20% HF. They were given a 1-hr anneal at 2400°C in argon; this treatment produced from one to five grains on the 5/8-in.-diam flat face. This anneal was followed by alternate abrasion through 4/0 metallographic paper and etching in 85% HNO_3–15% HF until no machining marks remained. Niobium-95 was deposited dropwise on the surface and evaporated to dryness.

Single-crystal specimens were alternately abraded and etched in the above solution until etching showed no evidence of residual strain. Specimens to be sectioned by grinding were used in this condition. For the anodizing and stripping technique, however, a polished surface was necessary. The specimens were electropolished in 90% H_2SO_4–10% HF at a current density of 1 to 2 amps/cm^2 for about 30 min. The isotope was deposited dropwise, electrodeposited, or vacuum evaporated from a tungsten filament. The efficiency of electrodeposition was marginal at best so that the other techniques were generally used. The specimens on which tracer atoms had been deposited by vacuum evaporation were somewhat easier to section by the stripping technique. At high temperatures the method of isotope deposition did not appear to affect the measured diffusivity, but in several specimens heat treated at temperatures less than 1200°C dropwise deposition seemed to cause erroneously high values.

Certain samples had ^{182}Ta codeposited with the ^{95}Nb. Since the gamma peaks are well separated in the spectrum, simultaneous measurements of diffusivity for both isotopes were possible.

Diffusion Anneals. – Diffusion anneals at temperatures greater than 1200°C were carried out in a tantalum resistance furnace in high-purity argon or in a vacuum of about 10^{-5}torr. Argon was used at very high temperatures to decrease evaporation of the specimen. Temperature control was manual but satisfactory because of short annealing times and

very small line-voltage fluctuations. Temperatures were read with a micro-optical pyrometer which had been calibrated against Pt vs Pt–10% Rh thermocouples to 1600°C. Corrections for higher temperatures were made by an extrapolation. Absolute accuracy of temperature measurements is estimated to vary between ±20° at 2400°C and ±5° at 1200°C.

Diffusion anneals at temperatures below 1200°C were carried out in a horizontal tube furnace with a Mullite tube under a vacuum of about 10^{-6} torr. Temperatures were controlled to ±1°C and measured with calibrated Pt vs Pt–10% Rh thermocouples.

Sectioning. – After the diameters were reduced by machining (to remove any surface effects), the specimens were sectioned by one of three techniques. The technique used for a particular sample is noted in the results. Lathe sectioning was done by standard methods. The section thickness was determined by weighing the collected chips. Grinding was done by hand on metallographic paper, the grade dependent on the section thickness desired. Figure-eight strokes were made on a marked paper area, and the samples were cleaned with alcohol and Kleenex. All paper was then taped together for counting. Section thicknesses were determined by weighing the specimen before and after grinding. Reliable sections as thin as 0.7 μ could be taken. The anodizing and stripping technique used to section low-temperature specimens has been described previously.[11] The minimum section thickness removable by this method was about 200 A; thus, D values as low as 10^{-19} cm^2/sec could be conveniently determined. Section thicknesses, which were determined from a calibration by Pawel, are directly proportional to anodizing voltage and almost independent of time for t >30 sec. The proportionality constant used was 9.51×10^{-8} cm/v, which is referred to the thickness of metal before anodization. This value was consistent with a direct measurement of a partially stripped specimen in a Zeiss interference microscope.

Counting. – Sections were counted by analyzing the 0.76 Mev gamma from ^{95}Nb (or the 1.1 and 1.2 Mev gammas from ^{182}Ta) using a single-channel gamma spectrometer with a 3- × 3-in. NaI(Tl) crystal. Gammas of 0.66 to 0.86 Mev (^{95}Nb) were counted; the background at this setting was about 0.6 cps. For samples on which both isotopes were deposited,

suitable corrections calculated from an experimental calibration of the background contribution of the unwanted isotope were made. These corrections were kept to a minimum by adjusting the ^{95}Nb-to-^{182}Ta ratio to about 10 during isotope deposition. Decay corrections were unnecessary for the treatment of these data.

Data Treatment. — The thin-film solution to the diffusion equation,

$$A(x) = \frac{M}{\sqrt{\pi Dt}} \exp\left(\frac{-x^2}{4Dt}\right), \qquad (3)$$

where A(x) is the specific activity at a distance x from the surface, D the diffusion coefficient, t the annealing time, and M a constant equal to the total activity originally deposited per unit area, was used to fit all data in this study. Recently, Mortlock[12] has reemphasized the fact that it is necessary to fulfill isotope layer thickness and solubility requirements in order for Eq. (3) to be applicable. It appears that these requirements were satisfactorily met in our work. Thus, data plotted as $\ell n\ A(x)$ vs x^2 should yield a straight line with a slope of $-1/4Dt$. The distance values were corrected for the change in density between room temperature and the diffusion temperature by using the linear expansion values of Krikorian.[13]

Some of the data were treated with a computer program written by one of the authors.[14] This program automatically plots the experimental points and draws the least-squares fit. In addition to the diffusion coefficient, the program computes the 90% confidence limits using Student's t test. The results were plotted on an Arrhenius-type plot and the activation energy and preexponential factor calculated by the method of least squares.

Results

Typical penetration plots of experimental data are given in Figs. 4.1 to 4.4. Figure 4.1 shows a plot for a lathe-sectioned,

---

[12] A. J. Mortlock, Acta Met. 12, 675 (1964).

[13] O. H. Krikorian, Thermal Expansion of High-Temperature Materials, UCRL-6132 (Sept. 1960).

[14] F. R. Winslow, A FORTRAN Program for Calculating Diffusion Coefficients and Plotting Penetration Curves, ORNL-TM-726 (Dec. 1963).

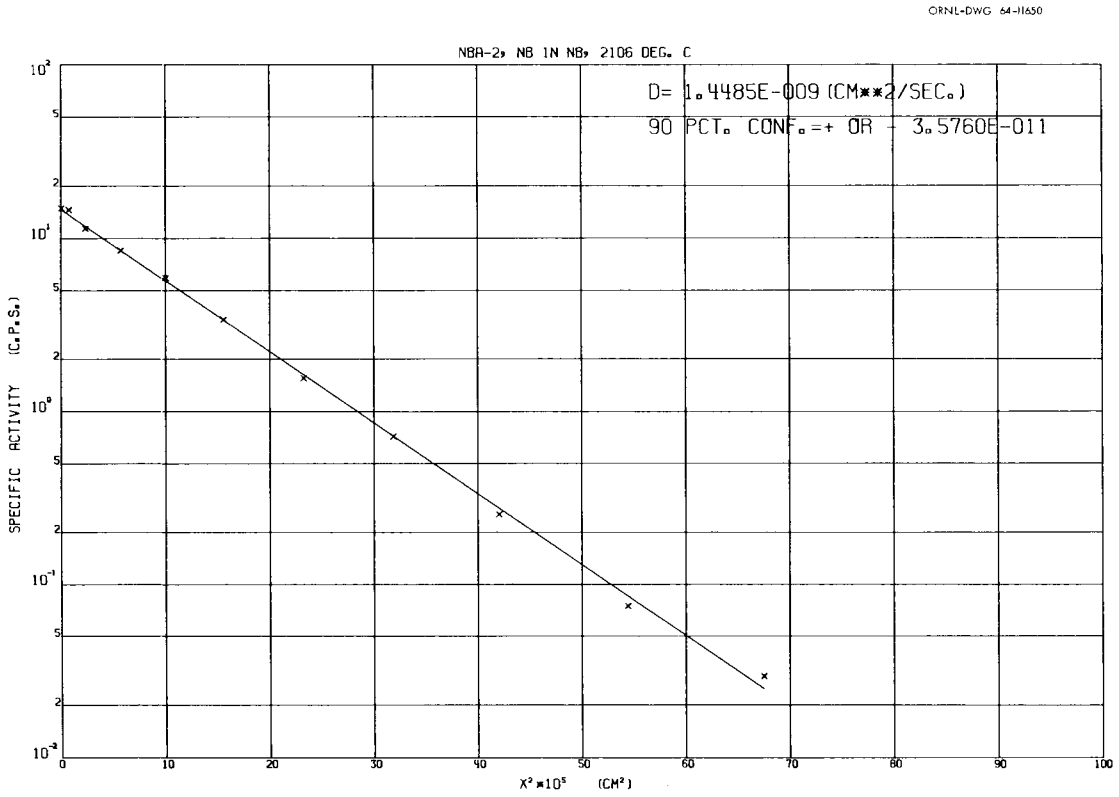

Fig. 4.1. Penetration Plot for a Polycrystalline Specimen Annealed 1.8×10^4 sec at 2106°C and Lathe Sectioned. Computer drawn plot.

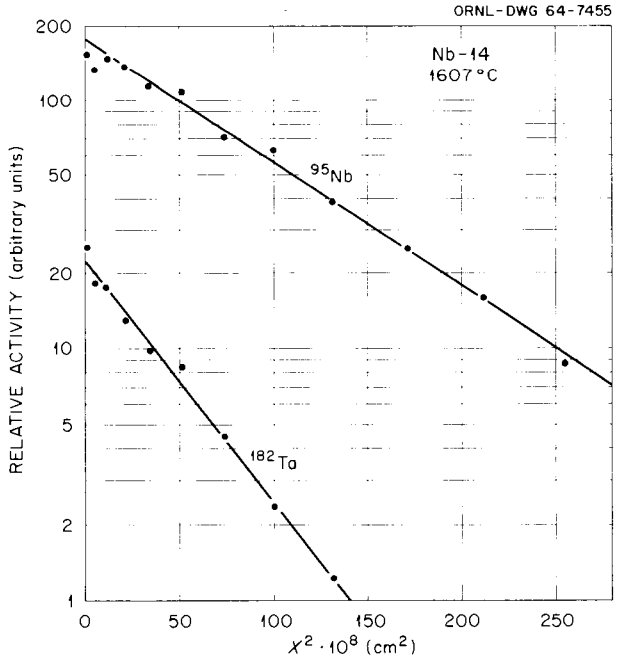

Fig. 4.2. Penetration Plot for a Single Crystal Annealed 2.6×10^4 sec at 1607°C and Sectioned by Grinding. Niobium-95 and tantalum-182 were codeposited on this specimen.

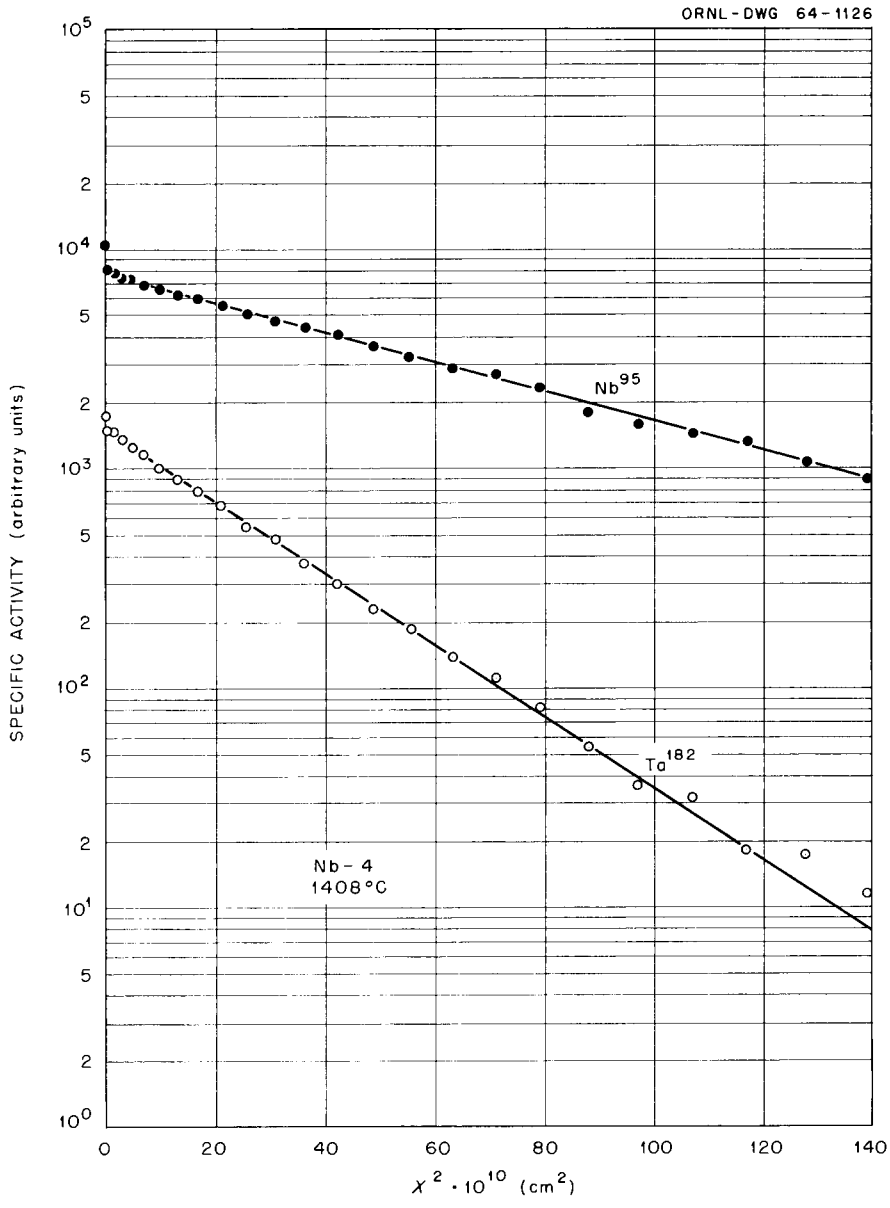

Fig. 4.3. Penetration Plot for a Single Crystal Annealed 7.4×10^3 sec at 1408°C and Sectioned by Anodizing and Stripping.

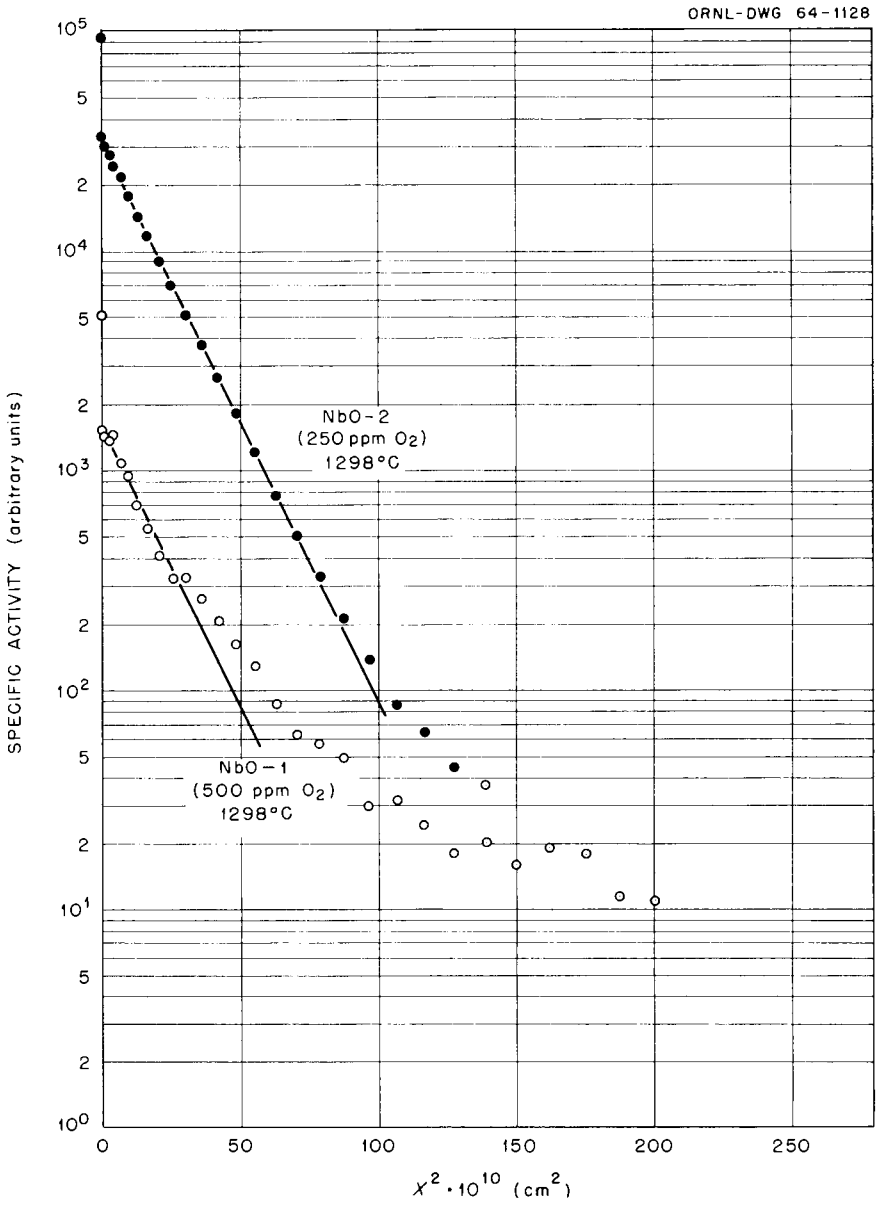

Fig. 4.4 Penetration Plot for Oxygen-Doped Single Crystals Annealed 9.3×10^3 sec at 1298°C. Sectioned by anodizing and stripping.

polycrystalline specimen. It is computer drawn by the previously mentioned program.[14] Figure 4.2 shows a plot for a single-crystal specimen sectioned by grinding. Both ^{95}Nb and ^{182}Ta were deposited on this specimen prior to the diffusion anneal, so that a simultaneous measurement of both diffusion coefficients was possible. Figure 4.3 shows a plot for a single-crystal specimen sectioned by the anodizing and stripping technique. Figure 4.4 contains results for oxygen-doped single crystals also sectioned by anodizing and stripping. The diffusion coefficients computed from the slopes of the penetration plots are listed in Table 4.3. Results of the experiments to determine the effect of oxygen on the self-diffusivity of niobium are given in Table 4.4.

The data for ^{95}Nb in niobium are summarized in an Arrhenius-type plot in Fig. 4.5. The best equation for a straight line through the data is

$$D_{Nb} = (1.10 \pm 0.04) \exp[-(96{,}100 \pm 1700)/RT] \text{ cm}^2/\text{sec} . \qquad (4)$$

Equation (2) holds for the entire temperature range covered in this investigation, 878 to 2400°C. The confidence limits on individual points are shown if they were large enough to be reproduced. For points which do not have error bars, the data point itself represents the 90% confidence interval. Several points, notably those at 1502, 1475, 1152, and 1103°C, were disregarded in the least-squares calculation. The reasons for discarding these points will be discussed later.

The data for diffusion of ^{182}Ta in niobium is shown with open circles in Fig. 4.5. The best straight line through the data is

$$D_{Ta} = 1.02 \exp(-99{,}300/RT) \text{ cm}^2/\text{sec} . \qquad (5)$$

Because of the limited amount of data, the standard errors were not calculated. It should be noted that the diffusion coefficients for tantalum in niobium are about a factor of 2 lower than the self-diffusivity of niobium. The activation energy and D_0, however, are quite similar. This apparent paradox may be resolved by the fact that the scatter present in the data leading to Eq. (5) was large enough so that it is not significantly different from Eq. (4). The factor of 2 difference between the

Table 4.3. Diffusion of ^{95}Nb and ^{182}Ta in Niobium

Temperature (°C)	Material and Sectioning Method	Diffusion Coefficient,[a] cm^2/sec		Root Mean Square Penetration[b] (μ)	Root Mean Square Relative Penetration[c]
		^{95}Nb	^{182}Ta		
2395	Polycrystal, lathe	$(1.90 \pm 0.03) \times 10^{-8}$		119.5	2.3
2320	Polycrystal, lathe	$(9.99 \pm 0.22) \times 10^{-9}$		89.1	1.8
2200	Polycrystal, lathe	$(4.04 \pm 0.21) \times 10^{-9}$		55.2	2.2
2140	Polycrystal, lathe	$(2.55 \pm 0.15) \times 10^{-9}$		43.8	1.8
2106	Polycrystal, lathe	$(1.45 \pm 0.04) \times 10^{-9}$		84.9	1.7
2073	Single crystal, grinding	$(9.60 \pm 0.33) \times 10^{-10}$	$(4.48 \pm 0.32) \times 10^{-10}$	29.0	4.1
2000	Polycrystal, lathe	$(8.95 \pm 0.48) \times 10^{-10}$		53.0	2.1
1999	Polycrystal, lathe	$(7.08 \pm 1.36) \times 10^{-10}$		53.0	2.1
1914	Single crystal, grinding	$(2.30 \pm 0.09) \times 10^{-10}$	$(1.34 \pm 0.07) \times 10^{-10}$	43.1	5.4
1899	Polycrystal, grinding	$(1.37 \pm 0.39) \times 10^{-10}$		41.0	5.9
1799	Polycrystal, grinding	$(6.43 \pm 0.55) \times 10^{-11}$		23.3	3.9
1776	Single crystal, grinding	$(5.42 \pm 0.21) \times 10^{-11}$	$(2.24 \pm 0.14) \times 10^{-11}$	19.8	5.6
1691	Polycrystal, grinding	$(2.66 \pm 0.41) \times 10^{-11}$		12.0	8.1
1673	Single crystal, grinding	$(1.75 \pm 0.13) \times 10^{-11}$	$(9.00 \pm 1.13) \times 10^{-12}$	11.3	4.0
1607	Single crystal, grinding	$(8.38 \pm 0.18) \times 10^{-12}$	$(4.13 \pm 0.29) \times 10^{-12}$	6.72	4.8
1601	Polycrystal, grinding	$(1.22 \pm 0.10) \times 10^{-11}$		7.07	5.1
1502	Polycrystal, grinding	$(5.82 \pm 0.64) \times 10^{-12}$		3.18	1.3
1475	Single crystal, grinding	$(3.17 \pm 0.23) \times 10^{-12}$	$(1.29 \pm 0.17) \times 10^{-12}$	2.83	1.6
1453	Single crystal, grinding	$(6.45 \pm 0.36) \times 10^{-13}$	$(2.46 \pm 0.27) \times 10^{-13}$	4.24	2.3

Table 4.3. (continued)

Temperature (°C)	Material and Sectioning Method	Diffusion Coefficient,[a] cm^2/sec		Root Mean Square Penetration[b] (μ)	Root Mean Square Relative Penetration[c]
		^{95}Nb	^{182}Ta		
1408	Single crystal, anodizing	$(2.01 \pm 0.05) \times 10^{-13}$	$(9.47 \pm 0.20) \times 10^{-14}$	0.59	12.5
1315	Polycrystal, anodizing	$(6.71 \pm 0.20) \times 10^{-14}$		0.39	4.1
1312	Polycrystal, anodizing	$(7.47 \pm 0.19) \times 10^{-14}$		0.40	4.2
1253	Single crystal, anodizing	$(2.16 \pm 0.03) \times 10^{-14}$	$(6.15 \pm 0.20 \times 10^{-15}$	0.31	5.4
1200	Single crystal, anodizing	$(6.27 \pm 0.36) \times 10^{-15}$		0.16	5.7
1152	Single crystal, anodizing	$(7.54 \pm 0.61) \times 10^{-15}$	$(5.46 \pm 0.30) \times 10^{-15}$	0.14	4.9
1103	Single crystal, anodizing	$(2.38 \pm 0.11) \times 10^{-15}$	$(1.53 \pm 0.07) \times 10^{-15}$	0.10	3.5
1077	Single crystal, anodizing	$(2.58 \pm 0.03) \times 10^{-16}$		0.12	4.2
1046	Single crystal, anodizing	$(8.21 \pm 0.42) \times 10^{-17}$		0.03	1.1
1001	Single crystal, anodizing	$(4.89 \pm 0.17) \times 10^{-17}$		0.06	2.0
951	Single crystal, anodizing	$(1.14 \pm 0.37) \times 10^{-17}$		0.02	0.85
878	Single crystal, anodizing	$(1.24 \pm 0.04) \times 10^{-18}$		0.014	0.57
878	Single crystal, anodizing	$(1.46 \pm 0.08) \times 10^{-18}$		0.014	0.57

[a] The accuracies shown are 90% confidence limits.

[b] The root mean square penetration is calculated as $(2D_R t)^{1/2}$ where D_R is taken from the line of Fig. 4.5.

[c] The relative penetration is defined as the ratio of the root mean square penetration to the average section thickness.

Table 4.4 Effect of Oxygen on Self-Diffusion in Niobium.

Temperature (°C)	Oxygen Content (ppm)	Diffusion Coefficient (cm^2/sec)
1200	250	6.29×10^{-15}
1200	420	6.29×10^{-15}
1298	250	4.70×10^{-14}
1298	420	4.70×10^{-14}
1501	250	1.16×10^{-12}
1501	420	1.16×10^{-12}

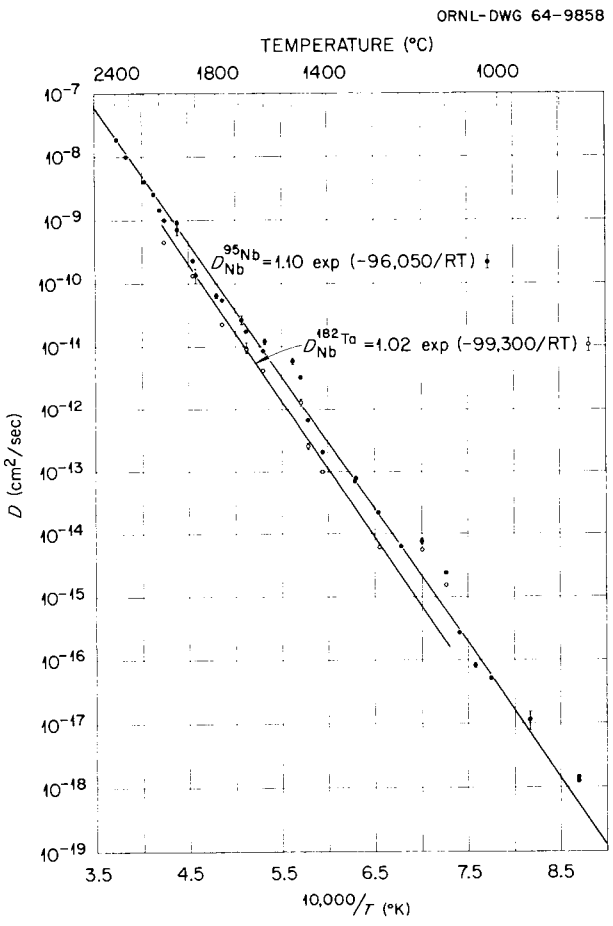

Fig. 4.5 Arrhenius Plot for Diffusion of ^{95}Nb and ^{182}Ta in Niobium.

^{95}Nb and ^{182}Ta diffusivities then seems to be a more sensitive method of describing the data than does a comparison of D_0 and Q values. A comparison of the results as a function of oxygen contents between 100 and 450 ppm shows that oxygen variations in this range cause no appreciable effect on self-diffusion in niobium.

Discussion

The present data for self-diffusion in niobium are in excellent agreement with the previous results of Resnick and Castleman[15] and Peart, Graham, and Tomlin.[16] However, the temperature range of the new data, 878 to 2400°C, is much wider than has previously been studied. The Arrhenius-type plot, Fig. 4.5, shows that an excellent straight line can be drawn through most of the data over the entire range, 10 orders of magnitude in D. There are, however, some data points not consistent with this straight line. It is our opinion that the points that do not fall on the line represent a real failure of the sectioning technique for diffusion studies, not simply experimental scatter.

Typical penetration plots such as those shown in Figs. 4.1 to 4.4 consisted of two regions. The initial region, from which most of the data given in Table 4.3 and shown in Fig. 4.5 were taken, was straight in a ℓn A(x) vs x^2 representation. Beyond a certain point, however, the experimental points showed a consistently higher activity than was given by the straight line through the data in the initial portion. The depth at which this upward deviation occurred and its magnitude varied from sample to sample. Generally, the "tail" was more prominent for polycrystalline samples than for single crystals and also was more prominent at lower temperatures. Material transport in this deeper region is presumably due to diffusion down dislocation short circuits.

---

[15]R. Resnick and L. S. Castleman Trans. Met. Soc. AIME 218, 307 (1960).

[16]R. F. Peart, D. Graham, and D. H. Tomlin, Acta Met. 10, 519 (1962).

Brown and Blackburn[17] have recently emphasized the importance of the resolution of a particular experimental technique. For any sectioning method the resolution is limited because the thickness of the cuts taken is finite. This consideration has been treated by Shirn, Wajda, and Huntington[18] who arrive at a result which may be summarized as:

$$\frac{d\,[\ell n\, A(x)]}{d\,x^2} = -\frac{1}{4Dt}\left[1 + \frac{h^2}{24Dt} + \ldots\right], \qquad (6)$$

neglecting any terms arising due to nonparallelism of the sections. In this equation, h is the section thickness and terms in h^4 and higher have been neglected. We now define the root mean square relative penetration (see Table 4.3) as $(2\,D_R t)^{1/2}/h$ where D_R is the true diffusivity. The root mean square relative penetration is a measure of the resolution of a particular sectioning technique. To measure the resolution, it is necessary to have the true diffusivity already known or to show that D is not changing with annealing time. For our case, we can assume with considerable experimental justification that the true diffusivity is represented by the straight line on the Arrhenius-type plot, Fig. 4.5. Note that the root mean square relative penetration is of the same form as the correction term in Eq. (6). If we allow D to vary by 20% (a reasonable variation in D for an Arrhenius plot covering such a wide temperature span), the root mean square relative penetration must be greater than 0.9 for the error due to finite section thickness to become important. All points except those at the two lowest temperatures are well within this criterion so this correction is not significant.

However, there are data points lying well above the line. We propose another correction which also is a function of the resolution of the sectioning technique but which is only present when the penetration

---

[17]A. F. Brown and D. A. Blackburn, Acta Met. 11, 1011 (1963).

[18]G. A. Shirn, E. J. Wajda, and H. B. Huntington, Acta Met. 1, 518 (1953).

plot shows the presence of a "tail", presumably due to dislocation and/or grain-boundary short circuiting. Suppose the sample of Fig. 4.3 had been lathe sectioned. The first data point would have included all tracer transport by the process which we will identify later as volume diffusion. Any subsequent points would have contained only material transported by short circuits. However, a penetration plot might have looked quite normal, with only the first point above the line. The D calculated from this specimen would have been in error (higher than the true volume diffusion coefficient) by a large amount. That is to say, the resolution of the lathe-sectioning technique would not be an adequate observation of the true penetration in that particular sample. Examination of the penetration plots for the specimens at 1502, 1475, 951, and 878°C shows that a few (one to four) of the initial data points are higher than the line drawn through the remainder of the data. In most of these samples there are not enough points in the initial region to justify calculating a diffusivity, but in one specimen (1475°C) two different values could be calculated. The lower of the two values was taken from the slope of the initial part of the penetration plot. This value agrees very well with the straight line while the other value agrees well with some of the other data which indicate, upon examination, that the resolution of the sectioning technique has been exceeded. Approximate values of the root mean square relative penetration are tabulated in Table 4.3. It appears that values below about 1.7 yield diffusivities which are higher than normal so we suggest this as an empirical constant for diffusion studies conducted on well-annealed single crystals. Obviously, if the deeper region is caused by dislocation short circuiting, this number depends on the perfection of the crystal.

The above explanation covers all but two of the high data points, those at 1103 and 1152°C. These values, determined early in the study, presumably are high because of a failure in the boundary conditions necessary to apply the thin-film solution, Eq. (3). The isotope was deposited dropwise on these specimens and decomposed only partially during annealing, leaving a surface residue. Such a residue was not

present on the specimens annealed at higher temperatures, and all runs at lower temperatures were made with the isotope deposited by evaporation.

The experiments on the effect of oxygen on niobium self-diffusion were undertaken after a suggestion by Kidson[19] that oxygen contamination might cause a temperature-independent vacancy concentration which could lead to positive deviations from Arrhenius plots at low temperatures. At the time it was not clear that niobium did not exhibit such behavior. Therefore, the fact that oxygen has no effect on niobium self-diffusivity, at least in the range of 100 to 450 ppm, while interesting, is not conclusive evidence against Kidson's theory. It seems from an examination of these penetration plots that oxygen contamination tends to increase the short-circuiting contribution. However, since these crystals came from a different supplier, they may have had different dislocation structures; so the evidence is not complete.

The data for ^{182}Ta diffusion in niobium, while fragmentary, leads to an activation energy and a D_0 almost identical to that of niobium, but to D values lower by a factor of about 2, an observation which is not surprising considering the chemical similarity of the two metals.

Conclusions

1. The volume self-diffusivity of niobium can be represented by:

$$D = (1.10 \pm 0.04) \exp[-(96{,}100 \pm 1700)/RT] \text{ cm}^2/\text{sec}$$

over the temperature range 878 to 2400°C.

2. A limited amount of data indicates that the diffusivity of ^{182}Ta in niobium is about a factor of 2 lower than the self-diffusivity and can be represented as

$$D = 1.02 \exp(-99{,}300/RT) \text{ cm}^2/\text{sec} \quad .$$

3. Oxygen has little or no effect on the self-diffusivity of niobium over a range of oxygen contents from 100 to 450 ppm.

---

[19] G. V. Kidson, Can. J. Phys. 41, 1563 (1963).

4. The occurrence of short-circuit diffusion, presumably along dislocations, can lead to erroneously high D values when combined with a loss of resolution of the sectioning technique.

5. It is suggested that values of the root mean square relative penetration be greater than 1.7 to avoid this loss of resolution.

Acknowledgments

The authors are grateful to T. L. Boswell, R. A. Padgett, and J. J. Campbell for their contributions to the experimental phases of this work. We wish to thank G. R. Love for reviewing the manuscript.

5. ZIRCONIUM METALLURGY

M. L. Picklesimer

We are conducting research along several lines on zirconium-base alloys of potential use as structural materials for water-cooled and/or -moderated reactor systems. The principal projects presently under way are: (1) studies of the physical metallurgy, consisting of transformation kinetics and morphologies, mechanical properties, phase diagrams, and heat-treatment response; (2) the development, evaluation, and utilization of preferred orientation and strain anisotropy in α-zirconium alloys during fabrication, and the utilization of yield stress anisotropy in increasing maximum permissible design stresses in structures; (3) the determination of the effects of composition, temperature, and environment on the oxidation-corrosion rates in the thin film states of oxide growth; (4) a study of the effects of alloy composition and oxidation environment on the structural properties of thin oxide films in situ; and (5) investigation of stress reorientation of hydrides in Zircaloy-2.

Anisotropy in Zircaloy-2

P. L. Rittenhouse M. L. Picklesimer

Tube Tester

The tube testing apparatus[1] for the study of strain anisotropy in Zircaloy-2 tubing is under construction. All of the parts being made in the machine shop have been heat treated preparatory to finish grinding. More than 90% of the parts have been finished. Assembly should be under way within two weeks. Debugging and preliminary testing are expected to be completed in the next quarter. A schematic operational diagram of the tube tester is given in Fig. 5.1.

---

[1] P. L. Rittenhouse and M. L. Picklesimer, Fuels and Materials Development Program Quart. Progr. Rept. Sept. 30, 1964, ORNL-TM-960, pp. 37 and 38.

ORNL-DWG 64-11633

TEST CAPABILITIES
Internal Pressure – 3000 psi
Torsion – 7500 lb-in, 360° Twist
Axial – 20,000 lb, 3 in Stroke

PROPERTY MEASUREMENT	
Property	Monitor
Axial Strain	LVDT, Camera
Torsion Strain	Potentiometer, Camera
Axial Stress	Load Cell
Torsion Stress	Load Cell
Internal Volume	LVDT

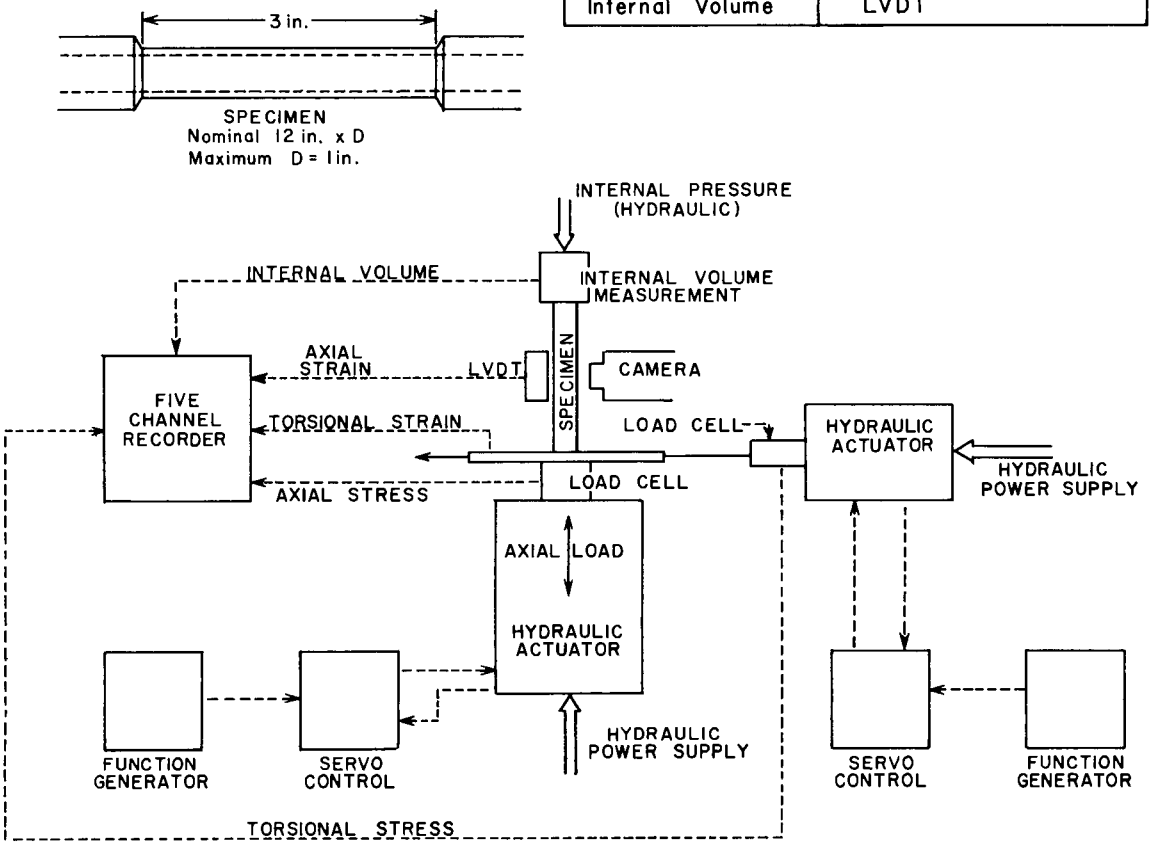

Fig. 5.1. Schematic Diagram of Tube Tester.

Tubing Fabrication Analysis

Analysis of the problem of controlling and moving texture during mill manufacture of tubing leads to a critical question: Is the orientation of the final material independent of the strain path when a given starting shape and texture is deformed into a given final shape? A corollary question is: Can a given shape change be accomplished by successive complete operations of the deformation systems known to operate in single crystals? Limited answers to both questions have been found, but the generality of these answers remains to be determined.

Consider the problem as presented in Fig. 5.2. First, assume that the specimen is a single-crystal cube with the basal plane parallel to one of the cube faces. The cube is to be distorted into an arbitrary shape which can be obtained by a simple sequence of successive twinning and/or slip operations. Next, both the shape and dimensional changes occurring when the cube is strained by path A of Fig. 5.2 and the new orientation of the basal pole are determined. Now, the problem is determining if exactly this shape and dimensional changes can be accomplished by another sequence of twinning and/or slip operations and if the location of the basal pole is the same or different. For the particular case of the shape and dimensional changes produced by path A, exactly the same changes can be made by path B (Fig. 5.2) with the additional result that the basal poles are essentially 90° apart. The dimensions of the shapes by the two paths are within 0.2% and the face angles agree within 1/2°.

Many combinations of final shapes and dimensions and of strain paths were examined. In general, if the final shapes and dimensions were the same by two apparently different paths, the basal pole orientations were found to be within 10° of each other. In many cases, no second path could be found which could produce the same shape and dimensional changes. Thus, only qualified and limited answers can yet be given to the two critical questions.

This analysis has shown some of the questions which must be continually asked during the planning of a fabrication sequence which is expected to control or move texture. For the particular sequences of Fig. 5.2, the two paths can be readily produced by mill equipment but it must be

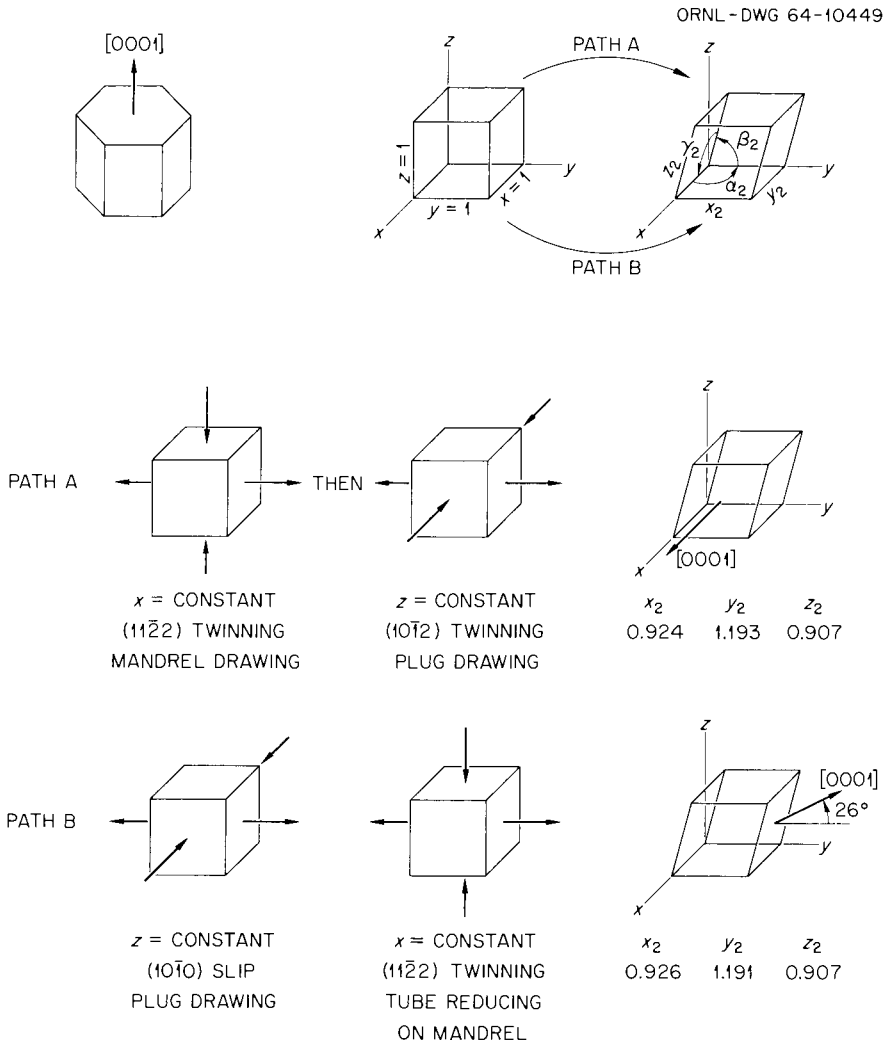

Fig. 5.2. Texture Change in Zirconium by two Strain Paths.

realized that only a specific and quite limited deformation of tubing can be obtained by these particular paths. It will thus be expected that the reduction or strain pattern of each step of the fabrication sequence will be controlled by the amount which will produce the desired change in texture and not by the amount of cold work the material can withstand before annealing is required.

Other combinations of deformation systems and shape changes will be examined to determine if any pattern can be detected which might lead to a conclusive general answer or decrease the amount of study required to obtain an answer when some particular shape, size, or texture change is desired.

Yield Anisotropy in Zircaloy-2

In the classical octahedral shear stress theory of plastic flow,[2] a yield ellipse is predicted for the case of plane stress (i.e., biaxial) in an isotropic material. It is assumed that the yield stress in tension is identical to that in compression, regardless of the test direction. Such behavior has generally been found for the cubic metals and a typical yield ellipse is shown in Fig. 5.3a. The yield strength in biaxial stress is the distance from the center to the ellipse boundary. Several cases of particular stress conditions ($\alpha = \frac{\sigma_2}{\sigma_1}$) are indicated on the figure by the letters A through H.

[2] A. Nadai, Theory of Flow and Fracture of Solids, vol 1, 2nd ed., pp. 209–213, McGraw-Hill, New York, 1950.

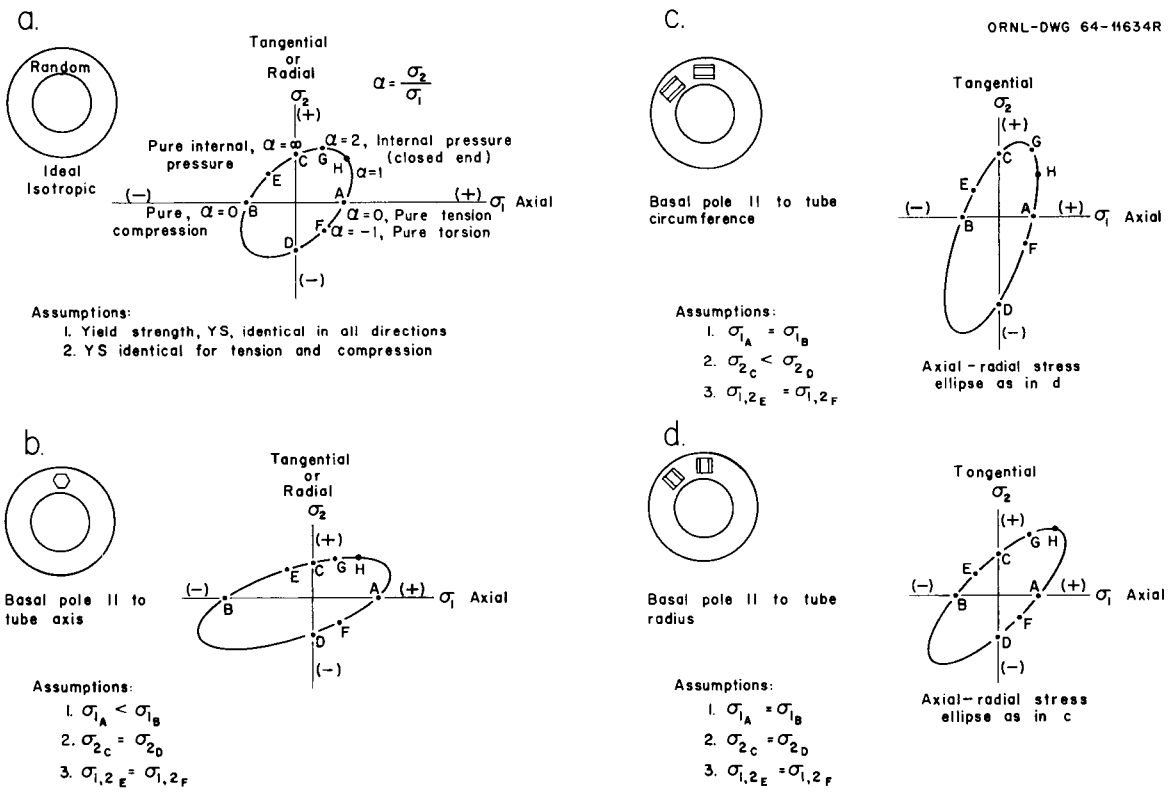

Fig. 5.3. Possible Yield Stress Ellipses for Zircaloy-2 in Biaxial Stress. Assuming (1) plane stress conditions (thin wall tubing) and (2) a modified octahedral shear stress theory is valid.

If the material is cubic and can be made to have an anisotropy of yield stress (i.e., it is commonly found in cold rolled mill products of steels, aluminum alloys, copper alloys, etc., that the tensile yield strength in the transverse direction is greater than that for the rolling direction), the yield ellipse is rotated to some extent and the ellipticity can be appreciably increased. This means that the yield strength in biaxial stress will be increased above that for the isotropic case. The center of the yield ellipse is, however, still at the center of the reference axes.

We have attempted to determine what the shapes and orientations of the yield ellipses could be for certain textures in Zircaloy-2 tubing, assuming that the octahedral shear stress theory can be modified to allow a material to have a yield strength in tension appreciably less than that in compression, and for the differences to vary greatly as the stress directions are moved relative to the crystallographic directions. We postulated three textures in tubing (basal poles concentrated in the axial, tangential, and radial directions), and assumed yield values previously obtained for certain crystallographic directions in highly textured Zircaloy-2 sheet.[3] The results are shown in Fig. 5.3B, C, and D.

If the above assumptions are even approximately valid, the yield ellipses for basal poles concentrated in the axial and tangential directions are not centered on the reference axes and are rotated so that the maximum yield strengths in biaxial stress do not occur for $\alpha = 1$ (internal pressure in a spherical pressure vessel, or in a bulge of a tube yielding to internal pressure) as is the case for isotropic material and for basal poles concentrated in the radial direction. In addition, the ellipticity of the yield ellipses is considerably greater than that found for the most anisotropic cubic metal.

Some important conclusions can be drawn as to the effects of the textures for certain stress conditions encountered in service. Consider the case of a closed end, internally pressurized tube as a bulge begins

---

[3]M. L. Picklesimer, A Preliminary Examination of the Formation and Utilization of Texture and Anisotropy in Zircaloy-2, ORNL-TM-460, p. 4 (Feb. 28, 1963).

to form in the wall. For the main portion of the tube, the stress condition is such that $\alpha = 2$ (point G). In the bulge itself, the stress condition is approaching that of $\alpha = 1$ (point H), the case of a spherical pressure vessel under internal pressure. If the texture is such that the basal poles are concentrated in the axial direction, Fig. 5.3B, the yield strength will be relatively low ($\alpha = 2$); and as the bulge forms, the stress required to yield will increase moderately rapidly (ignoring strain hardening). If the basal poles are concentrated in the tangential direction, Fig. 5.3C, the formation of the bulge will be catastrophic because the stress required for yielding ($\alpha = 1$) in the bulge is considerably less than that required for yielding to begin in the main body of the tube ($\alpha = 2$). This will be so even if a moderate amount of strain hardening occurs with increased plastic flow. This texture is that most commonly found in Zircaloy-2 tubing made for use as pressure tubing and fuel element cladding. The texture most resistant to bulging is that with basal poles concentrated in the radial direction (Fig. 5.3D) as the stress required for yielding increases rapidly as α goes from 2 to 1 (from the main part of the tubing to the bulge).

One of the first results to be obtained with the tube testing device now being constructed is a determination of the shape of the yield ellipse, particularly in the tension-tension quadrant.

One of the surprising results of the past studies of anisotropy in Zircaloy-2 plate and sheet was that the tensile strength (maximum load per original cross-sectional area) was essentially independent of texture,[4] (i.e., the material was almost isotropic in tensile strength). If now a "tensile strength ellipse" is plotted on the same axes as the yield stress ellipse, it can readily be seen that the "flow stress" ellipses must progressively rotate and move toward the center of the reference axes as plastic strain occurs. The "flow stress" ellipses increase in

---

[4]P. L. Rittenhouse and M. L. Picklesimer, Metallurgy of Zircaloy-2 Part II. The Effects of Fabrication Variables on the Preferred Orientation and Anisotropy of Strain Behavior, ORNL-2948 (Jan. 11, 1961).

size with plastic strain because the flow stresses required to continue strain increase as the material work hardens. Such analyses will be made shortly, using the stress-strain data previously obtained on textured Zircaloy-2 plate and sheet.

Oxide Film Studies

J. C. Banter

Previous results[5] indicated that the refractive index of anodic oxide films stripped from zirconium was lower than that of the films in place on the metal. Due to certain assumptions made in calculating the refractive indices of the *in situ* films, this reported difference must be considered to be only qualitative at present. We felt that a quantitative determination should be made directly on the *in situ* films, and have devised a suitable method. The technique involves the measurement by a spectrophotometer, using 10 and 60° angles of incidence, of the reflection interference patterns developed by a series of specimens anodized at successively higher voltages. Special specimen holders for these measurements were designed and are now being built.

This same technique will be used to determine the effects of irradiation on the refractive indices of these films. Two sets of identical specimens were prepared by anodizing strips of zirconium foil at voltages ranging from 50 to 400 v. One set has been canned and is currently being irradiated in an experimental facility at the ORR. It will be used in comparison with the unirradiated set to determine the effects of irradiation on the optical properties. These measurements should be completed during the coming quarter.

Preparation of Single Crystals of Zirconium and Zirconium Alloys

J. C. Wilson

Six zirconium spheres 3/8 to 5/8 in. in diameter were produced by electrical discharge machining from zone-refined stock. Two spheres were single crystals and each of the others contained at least one grain

---

[5]J. C. Banter, *Fuels and Materials Development Program Quart. Progr. Rept. Sept. 30, 1964*, ORNL-TM-960, pp. 46–48.

(covering 1/5 or more of the surface) in which $\{10\bar{1}0\}$, $\{11\bar{2}0\}$, and $\{0001\}$ poles could be seen. The spheres will be used to study the optical anisotropy of zirconium and the effect of orientation on oxidation and corrosion.

Orientation by visual inspection has been found possible for single crystal or large-grained spheres because the chemical polishing solution (46 H_2O, 46 HNO_3, 8 HF, parts by volume) produces matte areas of distinctive shape around the $\{10\bar{1}0\}$poles by pitting and faceting. Hydride platelets can also be used for orientation if they are observable. Combinations of both have confirmed that $\{10\bar{1}0\}$ is the habit plane for zirconium hydride in alpha zirconium.

Annealing in a high-purity argon atmosphere after crystal growth has frequently caused surface contamination of specimens. Use of a thick zirconium box with a tight lid has apparently eliminated contamination with oxygen and nitrogen but a small amount of hydrogen is still picked up by the specimens. The expendable lid is of 0.005-in.-thick zirconium foil which heats up rapidly in the furnace, gettering the argon inside the box before the box or the specimen heats enough to react with the gaseous impurities.

A more flexible and improved electrical discharge machining apparatus was designed and is now about 80% completed. It will be used for making spheres and tensile specimens from zone-refined single crystals and for cutting crystals to desired shapes and orientations.

Zone Refining of Zirconium

J. C. Wilson

The zone-refining apparatus and all utilities serving it were mounted on flexible mounts to minimize vibrations transmitted through the floor. The molten zone is now much more stable, a smoother surface is obtained on the specimens, the identification of the structure is easier, and the number of small stray grains on the surface is reduced. It also appears that, for reasons yet unknown, the thermal etching pattern on the specimens is much less prominent.

Several-zone refining runs of 10 passes each were made on short (zoned length less than 10 times the zone height) specimens to determine the effective distribution coefficients of hafnium and oxygen, the major impurities in zone-refined zirconium. Both elements have coefficients apparently just greater than one, and removal by zone refining may not be economical. Analytical results are not completed.

A mass-spectrometer residual gas analyzer (RGA) has been borrowed in order to determine the composition of the gases present during zone refining. The instrument is now being checked out on a portion of the new, ultra-high vacuum zone refiner being constructed. It is expected that the source of carbon contamination of the zone-refining systems (present even at pressures below 10^{-8} torr) can be identified and eliminated.

Properties of High-Purity Zirconium

J. C. Wilson

Annealing studies of zone-refined and iodide zirconium are in progress. This work will enable us to determine desirable heat treatment times and temperatures for corrosion and tensile specimens of zone-refined materials and perhaps give some insight to the vague concepts of recrystallization mechanisms in zirconium and its alloys.

Evidence that some recrystallization can occur in cold-rolled, zone-refined stock in 24 hr at 150°C was obtained by metallographic examination and confirmed by x-ray examination. For a given hardness in equal annealing times, the zone-refined zirconium requires an annealing temperature 250 to 300°C lower than values reported in the literature for iodide zirconium. The hardness of the cold-worked, zone-refined zirconium did not decrease monotonically with time at a given temperature in the range of 150 to 250°C. A hardness peak was observed in most specimens, but it is not now known whether the peak was due to age hardening or some other phenomenon. The hardness also became anisotropic as softening began. In the early stages of annealing, there appeared some metallographic evidence that elongated regions (perhaps deformation bands or recovered deformation bands) extended in the

rolling direction but the hardness anisotropy was often observed at higher temperatures where equiaxed structures were formed.

The various structures observed during the start of recrystallization are not easily reconciled with either the usual nucleation and growth mechanisms in metals or the generally accepted "recrystallization in situ" process in zirconium. We are presently trying to improve metallographic methods to resolve the partially recrystallized structures, and we expect to use both electron microscopy and x-ray diffraction techniques in an effort to determine and understand the structures produced.

Strip specimens from several parts of a zone-refined bar and a zone-refined sphere have been prepared for corrosion testing in 680°F water.

Previous reports in this series are:

ORNL-TM-920	Period Ending June 30, 1964
ORNL-TM-960	Period Ending September 30, 1964

Internal Distribution

1–3. Central Research Library
4–5. ORNL – Y-12 Technical Library Document Reference Section
6–15. Laboratory Records
16. Laboratory Records, RC
17. ORNL Patent Office
18. G. M. Adamson, Jr.
19. J. C. Banter
20. J. H. Barrett
21. S. E. Beall
22. M. Bender
23. R. G. Berggren
24. J. O. Betterton, Jr.
25. D. S. Billington
26. A. L. Boch
27. B. S. Borie
28. G. E. Boyd
29. W. H. Bridges
30. R. B. Briggs
31. W. E. Brundage
32. J. V. Cathcart
33. G. W. Clark
34. K. V. Cook
35. J. H. Crawford
36. J. E. Cunningham
37. J. H. DeVan
38. C. V. Dodd
39. D. A. Douglas, Jr.
40. J. I. Federer
41. B. E. Foster
42. A. P. Fraas
43. J. H Frye, Jr.
44. R. J. Gray
45. W. R. Grimes
46. J. P. Hammond
47. W. O. Harms
48. R. L. Heestand
49. M. R. Hill
50. N. E. Hinkle
51. H. W. Hoffman
52. H. Inouye
53. T. N. Jones
54. G. W. Keilholtz
55. B. C. Kelley
56. J. A. Lane
57. C. F. Leitten, Jr.
58. A. L. Lotts
59. T. S. Lundy
60. R. N. Lyon
61. H. G. MacPherson
62. R. E. MacPherson
63. M. M. Martin
64. W. R. Martin
65. R. W. McClung
66. H. E. McCoy, Jr.
67. H. C. McCurdy
68. R. E. McDonald
69. D. L. McElroy
70. C. J. McHargue
71. M. C. McIlwain
72. F. R. McQuilkin
73. A. J. Miller
74. E. C. Miller
75. F. H. Neill
76. S. M. Ohr
77. P. Patriarca
78. A. M. Perry
79. S. Peterson
80. M. L. Picklesimer
81. P. L. Rittenhouse
82. M. W. Rosenthal
83. G. Samuels
84. H. W. Savage
85. W. Schüle
86. J. L. Scott
87. O. Sisman
88. G. M. Slaughter
89. G. P. Smith, Jr.
90. S. D. Snyder
91. I. Spiewak
92. J. T. Stanley
93. W. J. Stelzman
94. J. O. Stiegler
95. A. Taboada
96. W. C. Thurber
97. D. B. Trauger
98. G. M. Watson
99. M. S. Wechsler
100. A. M. Weinberg
101. J. R. Weir
102. W. J. Werner
103. G. D. Whitman
104. J. M. Williams
105. R. O. Williams

106. J. C. Wilson
107. F. R. Winslow
108. H. L. Yakel, Jr.
109. F. W. Young, Jr.
110. C. S. Yust

External Distribution

111. A. J. Alexander, AEC, CANEL
112. R. J. Allio, Westinghouse Atomic Power Division
113. R. D. Vaker, Los Alamos Scientific Laboratory
114. L. Brewer, University of California, Berkeley
115. V. P. Calkins, GE, NMPO
116. W. Cashin, Knolls Atomic Power Laboratory
117. R. M. Cilimberg, Division of Reactor Development, AEC, Washington
118–119. D. F. Cope, AEC, ORO
120. G. K. Dicker, Division of Reactor Development, AEC, Washington
121. E. A. Evans, GE, Hanford
122. W. C. Francis, Phillips Petroleum Company
123. R. G. Grove, Mound Laboratory
124. D. H. Gurinsky, BNL
125. S. Hasko, NBS
126. A. N. Holden, GE, APED
127. J. S. Kane, University of California, Livermore
128. J. H. Kittel, ANL
129. E. J. Kreih, Westinghouse, Bettis Atomic Power Laboratory
130. W. L. Larsen, Iowa State University, Ames Laboratory
131. J. H. MacMillan, Babcock and Wilcox Company
132. R. E. Pahler, Division of Reactor Development, AEC, Washington
133. S. Paprocki, BMI
134. D. Ragone, GA
135. L. M. Raring, Pratt & Whitney, CANEL
136. Division of Research and Development, AEC, ORO
137. A. H. Roberson, U. S. Department of the Interior, Bureau of Mines
138. W. Rostokev, Illinois Institute of Technology Research Institute
139. F. C. Schwenk, Division of Reactor Development, AEC, Washington
140–141. J. M. Simmons, Division of Reactor Development, AEC, Washington
142. L. E. Steele, Naval Research Laboratory
143. R. H. Steele, Division of Reactor Development, AEC, Washington
144. W. F. Sheely, Division of Research, AEC, Washington
145. A. Strasser, United Nuclear Corporation

146. W. R. Voigt, Division of Reactor Development, AEC, Washington
147. C. E. Weber, Atomics International
148. G. W. Wensch, Division of Reactor Development, AEC, Washington
149. M. J. Whitman, Division of Reactor Development, AEC, Washington
150–164. Division of Technical Information Extension